PHYSICAL REVIEW D **79,** 084010 (2009)

Comparison of numerical and post-Newtonian waveforms for generic precessing black-hole binaries

Manuela Campanelli, Carlos O. Lousto, Hiroyuki Nakano, and Yosef Zlochower

Center for Computational Relativity and Gravitation and School of Mathematical Sciences, Rochester Institute of Technology, 78 Lomb Memorial Drive, Rochester, New York 14623, USA

(Received 5 August 2008; revised manuscript received 1 January 2009; published 6 April 2009)

We compare waveforms and orbital dynamics from the first long-term, fully nonlinear, numerical simulations of a generic black-hole binary configuration with post-Newtonian (PN) predictions. The binary has mass ratio $q \sim 0.8$ with arbitrarily oriented spins of magnitude $S_1/m_1^2 \sim 0.6$ and $S_2/m_2^2 \sim 0.4$ and orbits 9 times prior to merger. The numerical simulation starts with an initial separation of $r \approx 11M$ and orbital parameters determined by 2.5 PN and 3.5 PN evolutions of a quasi-circular binary starting from $r = 50M$. The resulting binaries have very little eccentricity according to the 2.5 PN and 3.5 PN systems, but show eccentricities of $e \sim 0.01$–0.02 and $e \sim 0.002$–0.005 in the respective numerical simulations, thus demonstrating that 3.5 PN significantly reduces the eccentricity of the binary compared to 2.5 PN. We perform three numerical evolutions from $r \approx 11M$ with maximum resolutions of $h = M/48$, $M/53.3$, $M/59.3$, to verify numerical convergence. We observe a reasonably good agreement between the PN and numerical waveforms, with an overlap of nearly 99% for the first six cycles of the ($\ell = 2$, $m = \pm 2$) modes, 91% for the ($\ell = 2$, $m = \pm 1$) modes, and nearly 91% for the ($\ell = 3$, $m = \pm 3$) modes. The phase differences between numerical and post-Newtonian approximations appear to be independent of the (ℓ, m) modes considered and relatively small for the first 3–4 orbits. An advantage of the 3.5 PN model over the 2.5 PN one seems to be observed, which indicates that still higher PN order (perhaps even 4.0 PN) may yield significantly better waveforms. In addition, we identify features in the waveforms likely related to precession and precession-induced eccentricity.

DOI: 10.1103/PhysRevD.79.084010 PACS numbers: 04.30.Db, 04.25.Nx, 04.70.Bw

I. INTRODUCTION

The discoveries of quasars, AGN, and other black-hole driven astrophysical phenomena in the 1960's demonstrated that the most energetic astrophysical phenomena are powered by gravity in the strong-field regime. This, in turn, spurred a renewed interest in classical general relativity. The second major milestone in the revival of the theory was the realization that when astrophysical black holes merge, they release incredible amounts of energy in the form of gravitational radiation, making them the brightest objects in the Universe. During their last few orbits, merging black-hole binaries release energy with a peak luminosity of about $10^{-3}c^5/G$, 10^{23} times the power output of the Sun.

There are currently major experimental and theoretical efforts underway to measure these gravitational wave signals. On the experimental side, these efforts required the construction of kilometers long interferometers, such as LIGO [1] and VIRGO [2], sensitive enough to measure arm length distance changes smaller than the radius of a proton. While on the theoretical side, these efforts required major advancements in signal extraction techniques and the theoretical modeling of the gravitational wave sources. Modeling the gravitational radiation from compact object sources has been particularly difficult, as they require solving the fully nonlinear Einstein equations of general relativity on powerful supercomputers. However, even with the rapid advancements in computer power, solving the two-body problem in general relativity proved to be remarkably difficult, requiring over 30 years of research for the field to mature. Then in 2005, two complementary and independent methods were discovered that allowed numerical relativists to finally solve the black-hole binary problem in full strong-field gravity [3–5].

The rapid progress and the number of new theoretical insights that followed these breakthroughs have transformed the field of numerical relativity (NR); turning it into a very valuable tool with significant impact on astrophysics [6–38], gravitational wave detection [39–53], and on our theoretical understanding of black-binary spacetimes [26,29,43,54–59].

One of the breakthrough methods, the ''moving puncture'' approach [4,5], was adopted by a majority of the NR groups and has proven to be accurate for the neutron-star binary and mixed neutron-star—black-hole binary problems [60,61], as well as for black-hole configurations with more than two black holes [62,63].

On the subject of black-hole binaries, the NR community is in very good agreement concerning a variety of results. Black-hole binaries will radiate between 2% and 8% of their total mass and up to 40% of their angular momenta, depending on the magnitude and direction of the spin components, during the last few orbits and merger [29,41–43]. In general, these binaries will radiate net linear momentum, causing the final remnant black hole to recoil

[6–29]. These recoils can be very large when the black holes in the binary have significant spin components in the orbital plane [15,18,20,64] (up to 4000 km s^{-1} for astrophysical binaries [20] and even 10 000 km s^{-1} for extremely close hyperbolic encounters [64]), which has astrophysically important effects [15,27,30–33]. The observational consequences of these large recoil velocities is an active area of current research [27,34–38].

Currently, one of the most important tasks of NR is to assist LIGO, VIRGO, and other interferometric observatories, in detecting gravitational radiation and extracting the physical parameters of the sources. Given the demanding resources required to generate these black-hole-binary simulations, and the sheer volume of the seven-dimensional space of intrinsic parameters of black-hole binaries, we need to develop techniques to model arbitrary binary configuration based on numerical simulations in a carefully chosen sample of the parameters space, in combination with post-Newtonian (PN) and perturbative calculations. One of the most promising of these approaches involves determining the region of common validity of the numerical simulations and post-Newtonian expansions, with the goal of modeling the full waveform using post-Newtonian waveforms for the initial inspiral and numerical waveforms for the late inspiral and merger. This method was pioneered with the use of the Lazarus waveforms [46] and has readily been pursued after the breakthroughs in NR.

Comparisons of numerical simulations with post-Newtonian ones have several benefits aside from the theoretical verification of PN. From a practical point of view, one can try to parametrize deviations of the current 3.5 PN expansions to fit the numerical results [65–69], or directly propose a phenomenological description [70], and thus make predictions in regions of the parameter space still not explored by numerical simulations. Another important application, from the theoretical point of view, is to have a calibration of the post-Newtonian error in the last stages of the binary merger. The first results of comparisons for equal-mass, nonspinning binaries are encouraging [48,49,71–73]. Recently this analysis was applied to equal-mass, equal-spin binaries with the spins aligned with the orbital angular momentum (and thus nonprecessing) [74–76].

In this paper we compare the numerical and post-Newtonian waveforms for the challenging problem of a generic black-hole binary, i.e. a binary with unequal masses and unequal, nonaligned, and precessing spins. The goal here is to evaluate accuracy of the current order of post-Newtonian expansions when including spins effects, as well as to develop new criteria for testing both numerical and post-Newtonian developments.

The paper is organized as follows. In Sec. II we review the numerical techniques used for the evolution of the black-hole binaries. In Sec. III we present results from the numerical evolution of two similar generic black-hole binaries, and in IV we analyze and compare different waveform modes as computed numerically and with the highest available post-Newtonian approximation. Finally, in Sec. V we present our conclusions.

II. TECHNIQUES

To compute the numerical initial data, we use the puncture approach [77] along with the TWOPUNCTURES [78] thorn. In this approach the three-metric on the initial slice has the form $\gamma_{ab} = (\psi_{\rm BL} + u)^4 \delta_{ab}$, where $\psi_{\rm BL}$ is the Brill-Lindquist conformal factor, δ_{ab} is the Euclidean metric, and u is (at least) C^2 on the punctures. The Brill-Lindquist conformal factor is given by $\psi_{\rm BL} = 1 + \sum_{i=1}^{n} m_i^p/(2|\vec{r} - \vec{r}_i|)$, where n is the total number of "punctures," m_i^p is the mass parameter of puncture i (m_i^p is *not* the horizon mass associated with puncture i), and $\vec{r}_i$ is the coordinate location of puncture i. We evolve these black-hole-binary data sets using the LAZEV [79] implementation of the moving puncture approach [4,5]. In our version of the moving puncture approach we replace the Baumgarte-Shapiro-Shibata-Nakamura (BSSN) [80–82] conformal exponent ϕ, which has logarithmic singularities at the punctures, with the initially C^4 field $\chi = \exp(-4\phi)$. This new variable, along with the other BSSN variables, will remain finite provided that one uses a suitable choice for the gauge. An alternative approach uses standard finite differencing of ϕ [5]. Recently Marronetti *et al.* [83] proposed the use of $W = \sqrt{\chi}$ as an evolution variable. For the runs presented here we use centered, eighth-order finite differencing in space [63] and an RK4 time integrator (note that we do not upwind the advection terms).

We use the CARPET [84] mesh refinement driver to provide a "moving boxes" style mesh refinement. In this approach refined grids of fixed size are arranged about the coordinate centers of both holes. The CARPET code then moves these fine grids about the computational domain by following the trajectories of the two black holes.

We obtain accurate, convergent waveforms and horizon parameters by evolving this system in conjunction with a modified 1 + log lapse and a modified gamma-driver shift condition [4,85], and an initial lapse $\alpha(t = 0) = 2/(1 + \psi_{\rm BL}^4)$. The lapse and shift are evolved with

$$(\partial_t - \beta^i \partial_i)\alpha = -2\alpha K, \tag{1a}$$

$$\partial_t \beta^a = B^a, \tag{1b}$$

$$\partial_t B^a = 3/4 \partial_t \tilde{\Gamma}^a - \eta B^a. \tag{1c}$$

These gauge conditions require careful treatment of χ, the inverse of the three-metric conformal factor, near the puncture in order for the system to remain stable [4,39,47]. In practice one sets a floor value for χ equal to one-tenth of its initial minimum value. This floor is only needed for the first $\sim 5M$ of evolution. As shown in Ref. [86], this choice of gauge leads to a strongly hyperbolic evolution system provided that the shift does not

become too large. In our tests, W showed better behavior at very early times ($t < 10M$) (i.e. did not require any special treatment near the punctures), but led to evolutions with lower effective resolution when compared to χ. We chose $\eta = 3$ for the simulations presented here.

We use AHFINDERDIRECT [87] to locate apparent horizons. We measure the magnitude of the horizon spin using the isolated horizon algorithm detailed in [88]. This algorithm is based on finding an approximate rotational Killing vector (i.e. an approximate rotational symmetry) on the horizon φ^a. Given this approximate Killing vector φ^a, the spin magnitude is

$$S_{[\varphi]} = \frac{1}{8\pi} \int_{\rm AH} (\varphi^a R^b K_{ab}) d^2V, \tag{2}$$

where K_{ab} is the extrinsic curvature of the 3D slice, d^2V is the natural volume element intrinsic to the horizon, and R^a is the outward pointing unit vector normal to the horizon on the 3D slice. We measure the direction of the spin by finding the coordinate line joining the poles of this Killing vector field using the technique introduced in [43]. Our algorithm for finding the poles of the Killing vector field has an accuracy of $\sim 2°$ (see [43] for details). Note that once we have the horizon spin, we can calculate the horizon mass via the Christodoulou formula

$$m^H = \sqrt{m_{\rm irr}^2 + S^2/(4m_{\rm irr}^2)}, \tag{3}$$

where $m_{\rm irr} = \sqrt{A/(16\pi)}$ and A is the surface area of the horizon.

We also use an alternative quasilocal measurement of the spin and linear momentum of the individual black holes in the binary that is based on the coordinate rotation and translation vectors [26]. In this approach the spin components of the horizon are given by

$$S_{[i]} = \frac{1}{8\pi} \int_{\rm AH} \phi^a_{[i]} R^b K_{ab} d^2V, \tag{4}$$

where $\phi^i_{[\ell]} = \delta_{\ell j}\delta_{mk} r^m \epsilon^{ijk}$, and $r^m = x^m - x^m_0$ is the coordinate displacement from the centroid of the hole, while the linear momentum is given by

$$P_{[i]} = \frac{1}{8\pi} \int_{\rm AH} \xi^a_{[i]} R^b (K_{ab} - K\gamma_{ab}) d^2V, \tag{5}$$

where $\xi^i_{[\ell]} = \delta^i_\ell$.

We measure radiated energy, linear momentum, and angular momentum, in terms of ψ_4, using the formulas provided in Refs. [89,90]. However, rather than using the full ψ_4, we decompose it into ℓ and m modes and solve for the radiated linear momentum, dropping terms with $\ell \geq 5$. The formulas in Refs. [89,90] are valid at $r = \infty$. We obtain highly accurate values for these quantities by solving for them on spheres of finite radius (typically $r/M = 50, 60, \cdots, 100$), fitting the results to a polynomial dependence in $l = 1/r$, and extrapolating to $l = 0$ [5,39,71,91]. Each quantity Q has the radial dependence $Q = Q_0 + lQ_1 + \mathcal{O}(l^2)$, where Q_0 is the asymptotic value [the $\mathcal{O}(l)$ error arises from the $\mathcal{O}(l)$ error in $r\psi_4$]. We perform both linear and quadratic fits of Q versus l, and take Q_0 from the quadratic fit as the final value with the differences between the linear and extrapolated Q_0 as a measure of the error in the extrapolations. We found that extrapolating the waveform itself to $r = \infty$ introduced phase errors due to uncertainties in the areal radius of the observers, as well as numerical noise. Thus when comparing PN to numerical waveforms, we use the waveform extracted at $r = 100M$. The extrapolations of the radiated quantities are far more robust.

We convert the (ℓ, m) modes of ψ_4 into (ℓ, m) modes of $h = h_+ - ih_\times$ by calculating the Fourier transform of each mode, dividing by $-\omega^2$ (where ω is the Fourier frequency), setting the value of the resulting transform to zero inside some specified window $-\omega_w < \omega < \omega_w$, as well as chopping off the transform at frequencies larger than 4 times the quasinormal frequency, and finally taking the inverse transform. By setting the transform to zero in this window, we remove the spurious constant and linear terms from h (we also remove spurious high-frequency noise from the waveform by truncating the transform at ~ 4 times the quasinormal frequency). We confirm that the calculation is correct by taking two time derivatives of the resulting h and measuring how much the resulting function differs from the original ψ_4 (see Fig. 5 in Sec. III). We also use an alternative waveform comparison, based on the modes of ψ_4 rather than h, which does not require this transformation.

We compute the eccentricities of the orbits using the techniques of [92] and introduce a second technique based on Newtonian trajectories. In [92], the eccentricity e_D is defined as

$$e_D(t) = \frac{r(t) - r_c(t)}{r_c(t)}, \tag{6}$$

where r_c is obtained by fitting $r(t)$ to a low-order polynomial in $t^{1/2}$. The actual eccentricity e_D is the amplitude of the oscillations in the resulting $e_D(t)$. We also introduce a second measurement of eccentricity e_r defined by

$$e_r(t) = r(t)^2 \ddot{r}(t)/M. \tag{7}$$

Here too, the eccentricity e_r is the amplitude of the oscillations in $e_r(t)$. This formula for the eccentricity, which is only accurate for $e \ll 1$, arises from the Newtonian formula for the orbital radius $r(t) = \sqrt[3]{M/\Omega^2}(1 + e\sin(\Omega t)) + \mathcal{O}(e^2)$. Note that in both cases, $e(t)$ has sinusoidal oscillations and secular decay. The ellipticity is the amplitude of the sinusoidal oscillations, while the secular decay affects the accuracy of the ellipticity calculation when its large. However, by differentiating $r(t)$ twice with respect to t, the secular terms are suppressed. Equation (7) can be modified with higher PN corrections

[93] to yield

$$e\cos(\Omega t) \approx [\ddot{r}(t) - \ddot{r}_0(t)]/(r\Omega^2), \tag{8}$$

where

$$\Omega^2 = \frac{M}{r^3}[1 - (3-\eta)(M/r) + \mathcal{O}(M/r)^2], \tag{9}$$

$$\dot{r}_0(t) = -\frac{64\eta}{5}\frac{M^3}{r^3}\left[1 - \frac{1}{336}(1751 + 588\eta)(M/r)\right], \tag{10}$$

$$\ddot{r}_0(t) = \frac{16\eta}{105}\frac{M^5}{r^4}[252 - (1751 + 588\eta)(M/r)], \tag{11}$$

and $r_0(t)$ is the zero-eccentricity inspiral trajectory.

A. Initial data

To generate the initial data parameters, we used random values for the mass ratio and spins of the binary (the ranges for these parameters were chosen to make the evolution practical). We then calculated approximate quasicircular orbital parameters for a binary with these chosen parameters at an initial orbital separation of $50M$ and evolved using purely PN evolutions until the binary separation decreased to $11M$. The goal was to produce very low-eccentricity orbital parameters at $r = 11M$, as suggested in [92]. This technique is rather different from the technique in [53], which used multiple numerical evolutions to determine quasicircular orbital parameters. The initial binary configuration at $r = 50M$ had $q = m_1/m_2 = 0.8$, $\vec{S}_1/m_1^2 = (-0.2, -0.14, 0.32)$, and $\vec{S}_2/m_2^2 = (-0.09, 0.48, 0.35)$. As described in Sec. IV, we used both truncated 2.5 PN equations of motion for spinning binaries, and equations of motions including 3.5 PN corrections (without the $H_{S_1S_2,3\,\mathrm{PN}}$ term). Our PN evolutions use the ADM-TT gauge which is the one closest to the numerical quasi-isotropic coordinates (to help reduce possible gauge ambiguities) [94,95]. We denote the two resulting configurations by G2.5 and G3.5, respectively. We then used the PN momenta, spins, and particle locations to construct the initial data for the numerical evolution. We fixed the puncture masses by requiring that the total ADM mass be $1M$ and that the mass ratio of the two holes has the specified value. We renormalized the parameters to obtain an ADM mass of $1M$ in order to aid comparison of the two configurations and the analysis.

The initial data parameter are summarized in Table I. We evolved these data using our eighth-order (in space) accurate code. We evolved the G2.5 configuration using 12 levels of refinement, with a finest resolution of $h = M/48$, $M/53.33$, and $M/59.33$, and the outer boundaries placed at $3072M$. We used the standard fifth-order Kreiss-Oliger dissipation operator and six buffer zones at the refinement level boundaries. For the timestep, we chose a CFL factor of 0.5 for the inspiral phase, and then dropped the CFL by a factor of 0.95 during the merger phase. We reduced the CFL because otherwise the simulation proved to be unstable during the very fast plunge phase (due to a violation of the CFL stability condition for our evolution system). We evolved the G3.5 configuration with the same setup as the $M/53.3$ G2.5 configuration, but chose an initial CFL factor of 0.475 (there was no evidence of any instability with this reduced factor).

III. FULLY NONLINEAR NUMERICAL WAVEFORMS AND TRAJECTORIES

We calculated ψ_4 using our original fourth-order accurate extraction code, and measured the convergence rate of the amplitude and phase of the waveform separately. In Fig. 1, we show the $(\ell = 2, m = 2)$ component of ψ_4 of the G2.5 configuration for the three resolutions. Note the excellent phase agreement until about $t = 1400M$. The phase error increases exponentially during the last two orbits. In Fig. 2, we show the convergence of the amplitude of the $(\ell = 2, m = 2)$ mode. The amplitude shows be-

TABLE I. Initial data parameters for the numerical evolutions. Parameters for configuration G2.5 were obtained from a truncated 2.5 PN evolution of a binary starting with an orbital separation of $r = 50M$, while parameters for configuration G3.5 were obtained from an evolution with 3.5 PN nonspinning corrections. The punctures have mass parameters m_i^p, horizons masses (Christodoulou) m_i^H, momenta $\pm\vec{p}$, spins $\vec{S}_i$, and both configurations have a total ADM mass M_{ADM}.

	G2.5	G3.5		G2.5	G3.5
m_1^p/M	0.406 59	0.406 94	m_2^p/M	4.123 28	0.456 072
m_1^H/M	0.448 41	0.448 33	m_2^H/M	0.560 54	0.561 06
x_1/M	3.327 70	−2.572 72	x_2/M	−2.662 16	2.058 67
y_1/M	−5.154 10	−5.570 57	y_2/M	4.123 28	4.456 96
z_1/M	0.518 35	−0.477 58	z_2/M	−0.414 68	0.406 45
S_1^x/M^2	0.017 896	−0.036 840	S_2^x/M^2	−0.066 727	0.025 826
S_1^y/M^2	0.069 204	−0.005 002 8	S_2^y/M^2	−0.098 217	0.149 51
S_1^z/M^2	0.034 786	0.069 584	S_2^z/M^2	0.147 22	0.110 50
p^x/M	0.072 919	0.080 499	p^y/M	0.048 074	−0.036 311
$10^3 p^z/M$	−5.4117	−0.743 105	M_{ADM}/M	1.000 00	1.000 00

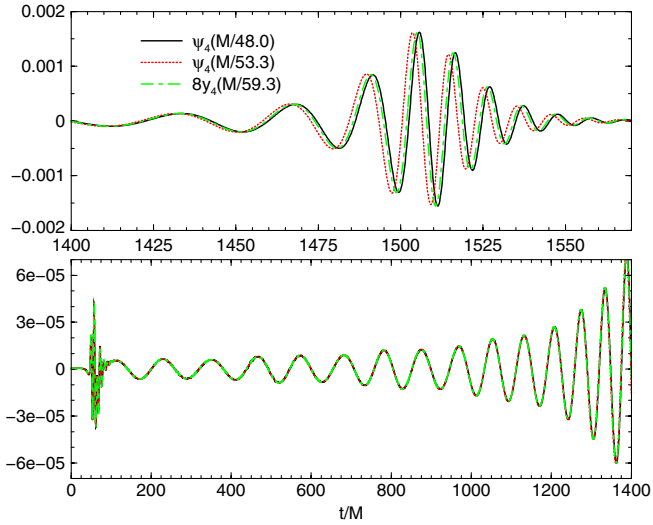

FIG. 1 (color online). The ($\ell = 2$, $m = 2$) component of ψ_4 for the G2.5 configuration for the three resolutions. Note the excellent phase agreement until about $t = 1400M$.

tween third- and fourth-order convergence as is apparent by rescaling the amplitude differences by 1.5098 (fourth-order) and 1.358 08 (third-order). As can be seen in Fig. 3, the phase error converges to eighth-order for $t < 1200M$. Beyond $t = 1200M$ (which is the beginning of the rapid plunge) the convergence falls to fourth-order, as is apparent from the rescaling of the phase differences by 2.305 73 (eighth-order), 1.5098 (fourth-order), and 1.358 08 (third-order). Note a convergence order of 8 (up to $t = 1200M$) implies that the error in the phase for the highest resolution run is less than 0.06 radians for $t < 1200M$. In Fig. 4, we show the amplitude as a function of phase. The phase error

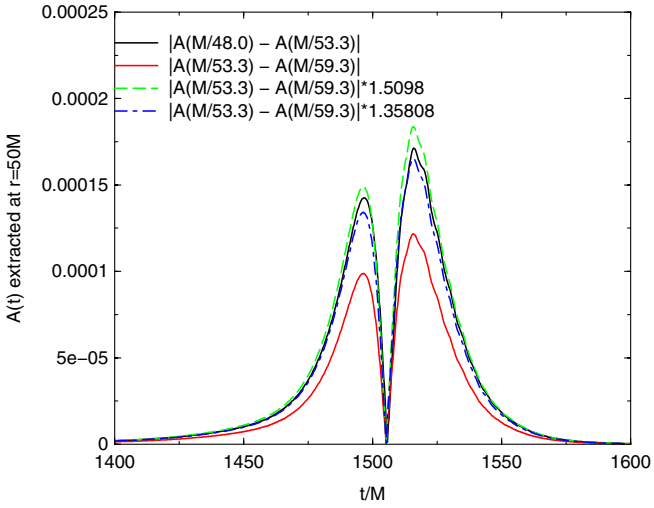

FIG. 2 (color online). Convergence of the amplitude of the G2.5 ($\ell = 2$, $m = 2$) component of ψ_4. The amplitude shows between third- and fourth-order convergence (as demonstrated by multiplying the deviations in the amplitude by 1.358 and 1.5098, respectively).

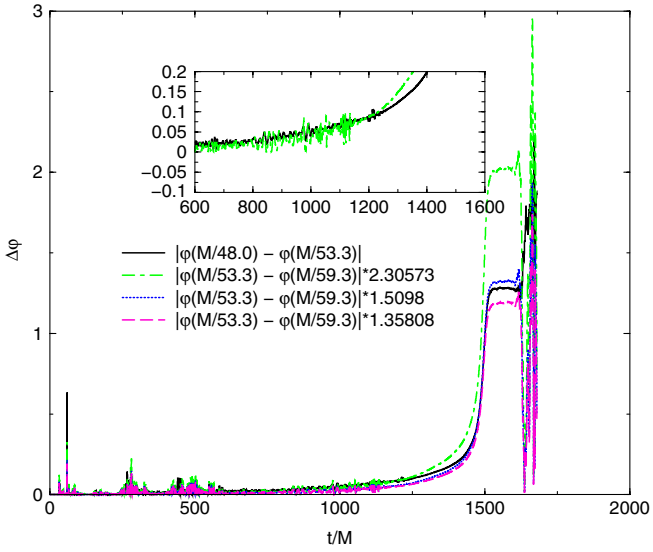

FIG. 3 (color online). Convergence of the G2.5 phase of the ($\ell = 2$, $m = 2$) component of ψ_4. The phase shows eighth-order convergence up to $t = 1200M$, decreasing to between third- and fourth-order convergence during the plunge (as demonstrated by multiplying the phase deviations by 2.305, 1.5098, and 1.358, respectively).

in the waveform converges to higher order than the amplitude because it is sensitive to the phase error in the orbit, which, in turn, is a function of the convergence of the evolution code. The amplitude, however, appears to be sensitive to the extraction algorithm's numerical error.

In Table II, we show the radiated energy, angular momentum, and gravitational recoil versus resolution for the G2.5 configuration [89,90]. Here, extrapolation errors (to infinite radius) in the radiated energy and angular momenta dominate the finite-difference errors, while the extrapola-

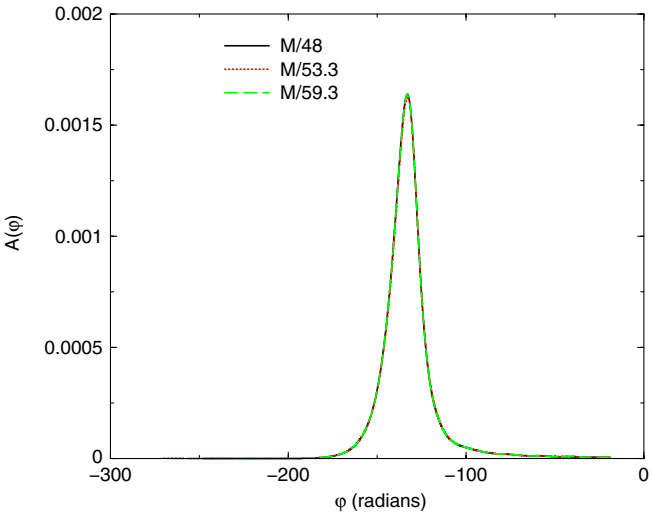

FIG. 4 (color online). The amplitude of the G2.5 ($\ell = 2$, $m = 2$) component of ψ_4 versus the phase. Note that the phase becomes more negative as t increases.

TABLE II. The radiated energy, angular momentum, and gravitational recoil versus resolution for the G2.5 configuration. The quoted uncertainties are due to extrapolation $r \to \infty$. Note that this configuration has eccentricity $e_D \sim 0.02$ and $e_r \sim 0.01$.

	$M/48$	$M/53.3$	$M/59.3$
$E_{\rm rad}/M$	0.0512 ± 0.0039	0.0513 ± 0.0036	0.0514 ± 0.0033
$J^x_{\rm rad}/M^2$	0.018 ± 0.021	0.017 ± 0.020	0.014 ± 0.013
$J^y_{\rm rad}/M^2$	-0.05 ± 0.12	-0.05 ± 0.12	-0.05 ± 0.13
$J^z_{\rm rad}/M^2$	0.4445 ± 0.0081	0.4478 ± 0.0103	0.4466 ± 0.0077
$V^x_{\rm rec}$ (km s^{-1})	-1.6 ± 5.7	-6.9 ± 6.0	-2.2 ± 5.5
$V^y_{\rm rec}$ (km s^{-1})	78.36 ± 6.51	75.75 ± 2.95	71.47 ± 0.24
$V^z_{\rm rec}$ (km s^{-1})	934 ± 31	1008 ± 24	947 ± 16

tion errors in the recoil appear to be similar to the finite-difference errors. In particular $V^z_{\rm rec}$ has a noticeable finite-difference error. This can be understood in terms of the sensitivity of the out-of-plane recoil to the angle that the spin direction makes with the infall direction at merger. Thus orbital phase errors in the plunge can lead to significant deviations in the out-of-plane recoil [96,97].

The radiated energy, angular momentum, and the recoil velocity for the G3.5 configuration are given in Table III. The radiated energy and angular momenta are slightly larger for the G3.5 configuration than the G2.5 configuration. Note that for both configurations, the radiated angular momenta in the x and y directions are too small to accurately measure. It should be pointed out that the quoted uncertainties in the radiated quantities for G3.5 are due to extrapolation to infinity. Additional uncertainties, due to truncation errors are not included (although results from G2.5 indicate that the uncertainties in the radiated energy and angular momentum due to truncation errors are small compared to the errors due to extrapolation).

As a final point, we show that our method for calculating h from ψ_4 using truncated Fourier transforms, yields a reasonable approximation to the original ψ_4 after differentiating twice. In Fig. 5, we show $\ddot{h}$ and ψ_4 of the subleading ($l = 2$, $m = 1$) mode of the G2.5 configuration (see however the discussion concerning the amplitudes of h in Sec. IV B 1).

TABLE III. The radiated energy, angular momentum, and gravitational recoil for the G3.5 configuration. The quoted uncertainties are due to extrapolation $r \to \infty$. Note that this configuration has eccentricity $e_D \sim 0.005$ and $e_r \sim 0.002$.

$E_{\rm rad}/M$	0.0522 ± 0.0042
$J^x_{\rm rad}/M^2$	-0.20 ± 0.27
$J^y_{\rm rad}/M^2$	0.051 ± 0.057
$J^z_{\rm rad}/M^2$	0.4551 ± 0.0029
$V^x_{\rm rec}$ (km s^{-1})	26.3 ± 5.2
$V^y_{\rm rec}$ (km s^{-1})	103.0 ± 5.7
$V^z_{\rm rec}$ (km s^{-1})	1529.9 ± 8.9

A. Eccentricity and precession

In Figs. 6–8, we show the orbital trajectory for the G2.5 and G3.5 configurations. With the time direction suppressed, we see excellent agreement between the trajectories at the three resolutions. This is similar to the excellent agreement in the amplitude versus phase of the ($\ell = 2$, $m = 2$) mode. However, when including time, as can be seen in Fig. 9, there is a significant difference between the high and medium resolutions for $t > 1200M$. Also note, in Fig. 9, the large eccentricity (apparent from the oscillations in r) for the G2.5 configuration and that G3.5 has reduced, but still large, eccentricity. Thus, assuming that the PN series converges, we need to include still a higher-order PN correction to obtain low-eccentricity initial data parameters. The reduced eccentricity of G3.5 compared to G2.5, lends support to the hope that a higher PN order will give low-eccentricity data. Alternatively, to produce low-eccentricity data, one can try to use the iterative methods of [53], which have been shown to work well for non-spinning binaries. Using the methods of [92], we can

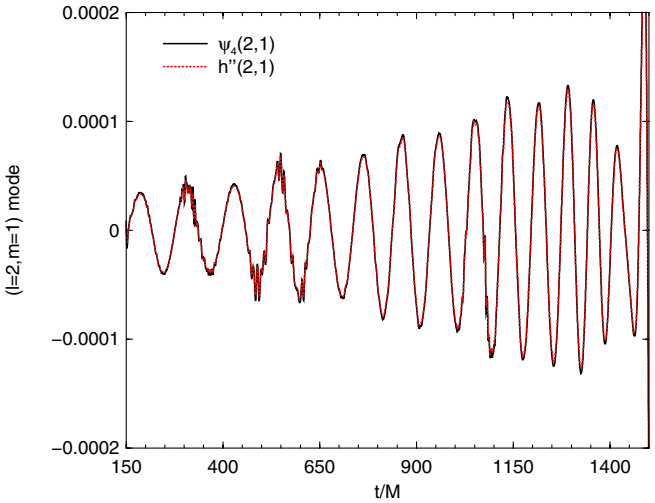

FIG. 5 (color online). A comparison of $\ddot{h}$ and ψ_4 for the ($\ell = 2$, $m = 1$) mode for the G2.5 configuration. The plot demonstrates that the windowing procedure apparently does not contaminate the waveform to a significant degree.

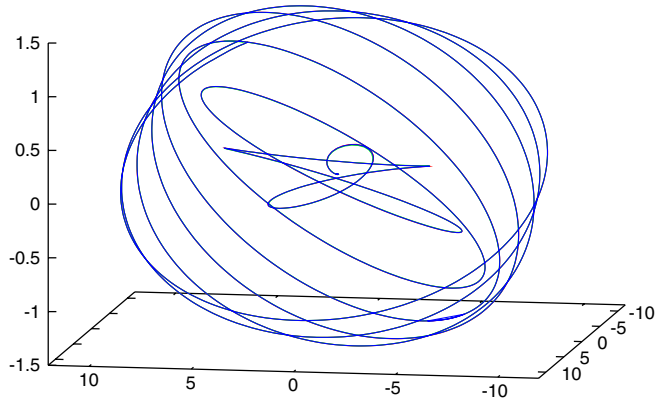

FIG. 6 (color online). The trajectory difference $\vec{x}_1$–$\vec{x}_2$ for the G2.5 configuration. Note the orbital plane precession and the very good agreement between trajectories at the different resolutions (the tracks from the different resolutions are not distinguishable on this scale).

calculate the eccentricity $e_D(t)$, as shown in Fig. 10. From the figure, we can see that the eccentricity of G2.5, which is $e_D \sim 0.02$, is more than 3.5 times as large as the eccentricity of G3.5, which is $\sim$0.005. Using the formula e_r for the eccentricities (see Fig. 11) yields $e_r \sim 0.0088$ for G2.5 and $e_r \sim 0.0022$ for G3.5. However, as can be seen in the figure, the eccentricity for G2.5 decays throughout the evolution, while the eccentricity of G3.5 (although smaller than G2.5) remains roughly constant for $t \gtrsim 600M$. This is consistent with the results seen in Fig. 16 which shows that

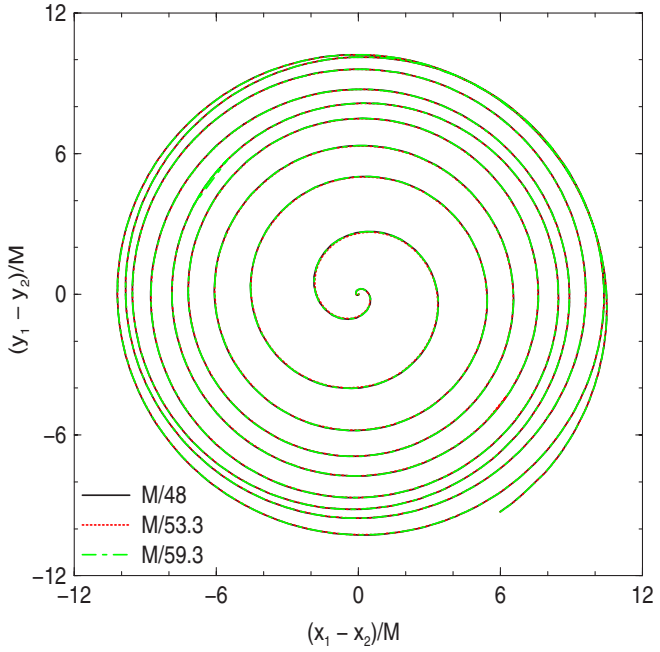

FIG. 7 (color online). An xy projection of the trajectory difference $\vec{x}_1$–$\vec{x}_2$ for the G2.5 configuration. Note the very good agreement between trajectories at the different resolutions. The initial orbital plane is inclined with respect to the xy plane, making the orbit appear more eccentric.

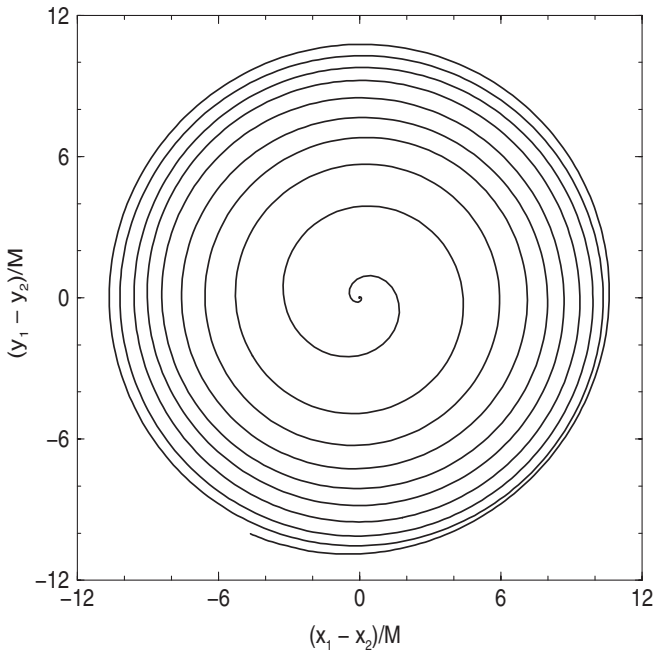

FIG. 8. An xy projection of the trajectory difference $\vec{x}_1$–$\vec{x}_2$ for the G3.5 configuration. The initial orbital plane is inclined with respect to the xy plane, making the orbit appear more eccentric.

the 3.5 PN prediction for the eccentricity does not decay with time for sufficiently close binaries and small eccentricities. In Ref. [92], they found that using PN parameters from a PN-evolved inspiral (from $r = 40M$ to $r = 11M$)

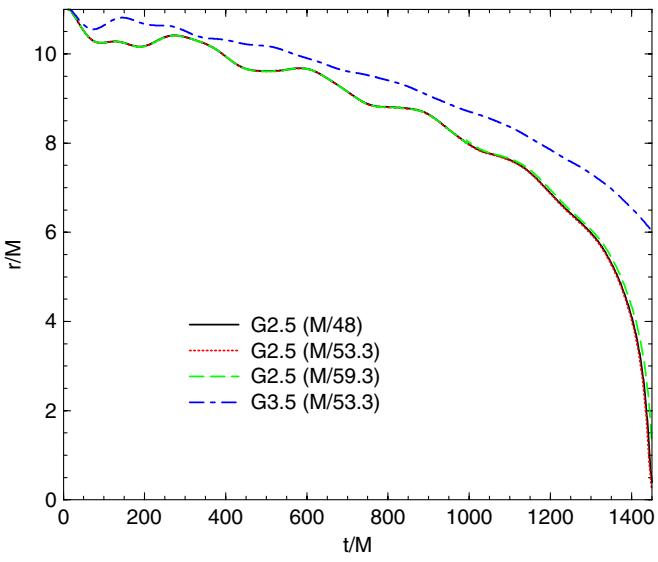

FIG. 9 (color online). The coordinate distance $r = |\vec{x}_1$–$\vec{x}_2|$ between punctures versus time for the G2.5 and G3.5 configurations. Note that the large eccentricity in the orbit (apparent in the oscillation in r) is reduced by using the 3.5 PN equations to generate the initial data. Unlike in Figs. 6 and 7, here the differences between resolution becomes apparent during the plunge. These differences drive the phase error. Also note that the G3.5 configuration merges more slowly.

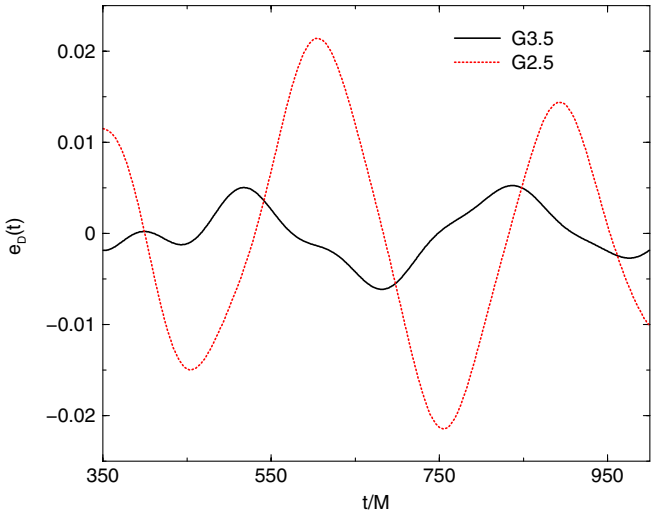

FIG. 10 (color online). The eccentricity $e_D(t)$ of the G3.5 and G2.5 configurations, as calculated using the techniques of [92].

reduced the eccentricity of the resulting binary from $e = 0.01$, for a quasicircular binary at $r = 11M$, to $e = 0.002$. Here we see eccentricities after a PN-evolved inspiral to $r = 11M$ between 2.5 and 10 times as big.

In Figs. 12 and 13, we show $\vec{r} = \vec{x}_1 - \vec{x}_2$ versus time for the G2.5 and G3.5 configurations after performing a constant rotation that maps the initial orbital motion onto the xy plane. Orbital plane precession drives the increase in amplitude of the z component of $\vec{r}$. The precession of the orbital plane is itself driven by the precession of the total spin of the binary. Thus we can measure the rate of orbital plane precession by looking at the components of the black-hole spins as a function of time. In Fig. 14, we show the components of the spin of the larger black hole as a function of time for the G3.5 configuration. Note that the precessional frequency is quite low, with the precession

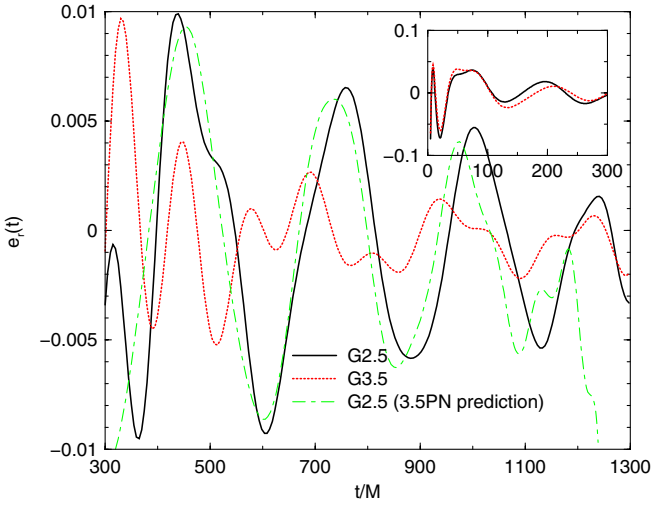

FIG. 11 (color online). The eccentricity $e_r(t)$ of the G3.5 and G2.5 configurations and the 3.5 PN prediction for the G2.5 configuration (the 3.5 PN prediction for G3.5 is a factor of 10 smaller than the NR prediction). The inset shows the "eccentricity" at early times when gauge effects dominate the trajectories. Note that the eccentricity of G2.5 decays throughout the evolution while the smaller eccentricity for G3.5 remains roughly constant beyond $t \sim 630M$. At later times the eccentricities of G2.5 and G3.5 begin to agree.

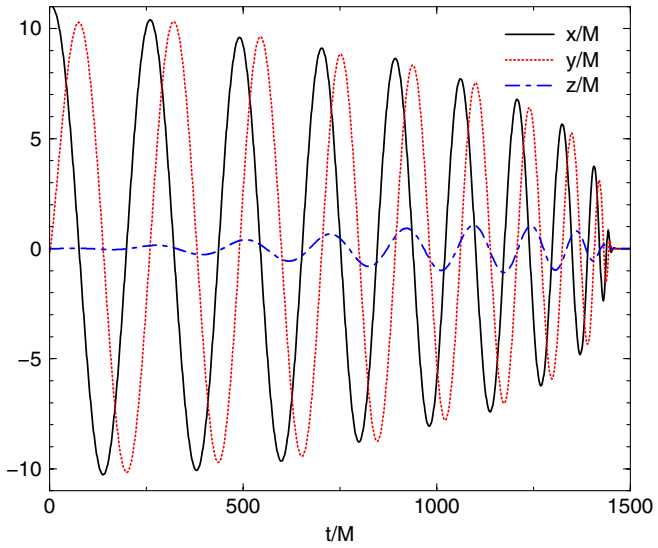

FIG. 12 (color online). The coordinate displacement $\vec{r} = \vec{x}_1 - \vec{x}_2$ between punctures versus time for the G2.5 configuration after performing a constant rotation that maps the initial orbital plane onto the xy plane. Precession is responsible for driving the amplitude of r^z.

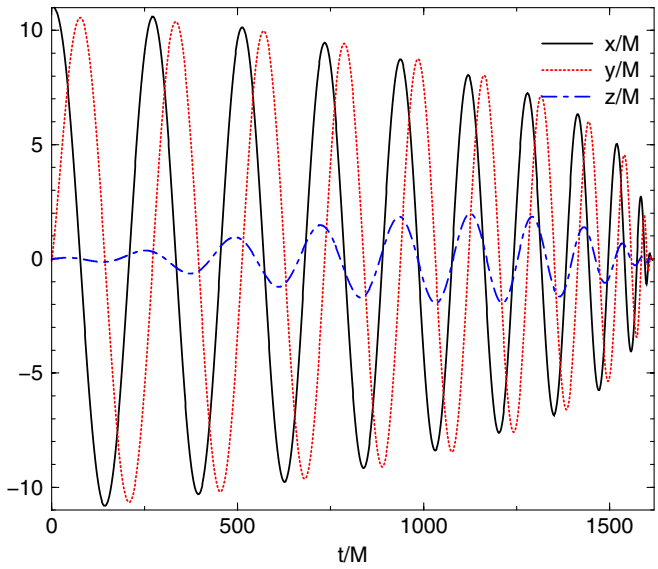

FIG. 13 (color online). The coordinate displacement $\vec{r} = \vec{x}_1 - \vec{x}_2$ between punctures versus time for the G3.5 configuration after performing a constant rotation that maps the initial orbital plane onto the xy plane. Precession is responsible for driving the amplitude of r^z.

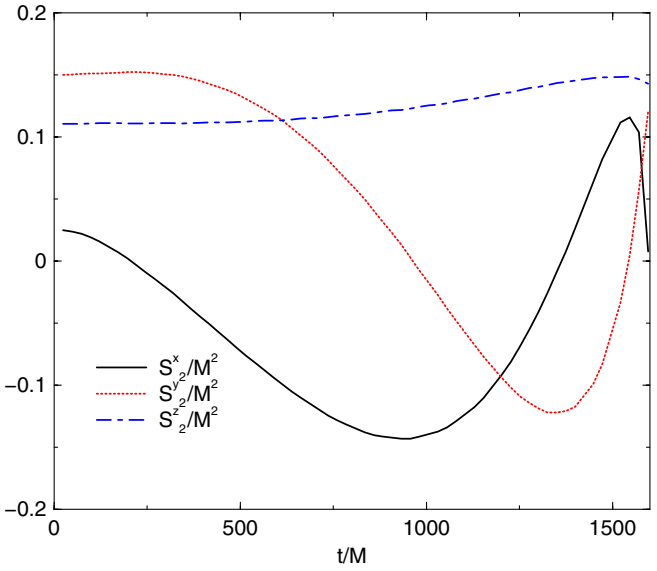

FIG. 14 (color online). The components of the spin for the more massive black hole in configuration G3.5 as a function of time. The precession of the spin drive the orbital plane precession. Here the precession time scale is of order $1000M$.

occurring on a time scale of order $1000M$; consistent with the time scale in the amplitude modulation of the rotated z_1–z_2 trajectory component in Figs. 12 and 13. Despite this long time scale, precession can affect the waveform modes on shorter time scales via mode-mixing effects. That is, precession of the orbital plane will cause our mode decomposition (which uses a fixed z axis) to mix different modes (which oscillate at different frequencies). This can lead to a beating effect that produces amplitude oscillations visible in the waveform. In particular, when the orbital plane is aligned with the xy axis, the m modes have a frequency of $\sim m\omega_{\rm orbit}$. Hence if the $m = 2$ and $m = 1$ or $m = 3$ modes mix, the resulting system will have a beat frequency of $\sim\omega_{\rm orbit}$; the same frequency as that due to eccentricity. Thus, oscillations in the amplitude of the modes at the orbital frequency can arise both from precession and ellipticity. We will come back to this point in Sec. IV B.

IV. POST-NEWTONIAN EQUATIONS OF MOTION AND WAVEFORMS

In order to calculate PN waveforms, we need to calculate the orbital motion of the binaries. We use the ADM-TT gauge, which is the closest to our quasi-isotropic numerical initial data coordinates [94,95]. In this paper, we use two different approximate PN equations of motion (EOM) based on [98–100]. To construct the EOM we use the Hamiltonian provided in [98], with the additional terms provided in [99,100], and the radiation-reaction force provided in [98]. We then use the standard techniques of the Hamiltonian formulation to construct EOM for the particle locations, momenta, and spins. In the first approximate EOM, we included the purely orbital Hamiltonian up to 2 PN order, spin-orbit coupling up to 2.5 PN order, and spin-spin coupling up to 2 PN order (for the conservative part). That is to say, we use the Hamiltonian

$$H^R = H_{\rm O,Newt} + H_{\rm O,1\,PN} + H_{\rm O,2\,PN} + H_{\rm SO,1.5\,PN} + H_{\rm SO,2.5\,PN} + H_{\rm SS,2\,PN}. \quad (12)$$

Here we only include the leading order radiation-reaction (dissipative) effect. We refer to the above EOM as the "truncated" 2.5 PN EOM because there are terms up to 2.5 PN order. For the second approximate EOM, we included the 3 PN orbital Hamiltonian and 3 PN spin(1)–spin(2) coupling in the ADM-TT gauge [100], i.e., we use the Hamiltonian

$$H^F = H^R + H_{\rm O,3\,PN} + H_{S_1S_2,3\,\rm PN} \quad (13)$$

(the $H_{S_1S_2,3\,\rm PN}$ term was also computed in [101–103] in a different gauge). For the dissipative part, we added the 3.5 PN (nonspinning) radiation-reaction terms, as well as the leading spin-orbit and spin-spin coupling to the radiation reaction [98]. In the radiation-reaction terms, we use the Taylor series of the flux [104,105]. We refer to this second EOM as the 3.5 PN EOM (in practice the 3.5 PN radiation-reaction terms contribute to the orbital EOM at 6 PN order).

We then use the following procedure to construct hybrid waveforms from the orbital motion. First we use the 1 PN accurate waveforms derived by Wagoner and Will [106] (WW waveforms) for a generic orbit. By using these waveforms, we can introduce effects due to eccentricity and effects due to black-hole spins, including the precession of the orbital plane. On the other hand, Blanchet *et al.* [107] recently obtained the 3 PN waveforms (B waveforms) for nonspinning circular orbits. We combine these two waveforms to produce a hybrid waveform that includes the known higher-order corrections to the waveform. Note that, in the comparisons mentioned below, the truncated 2.5 PN waveforms and the 3.5 PN waveforms were constructed from the same WW and B expressions. Differences only arise because the truncated 2.5 PN waveforms are based on particle trajectories obtained from the truncated 2.5 PN EOM.

In order to combine the WW and B waveforms, we need to take into account differences in the definitions of polarization states and the angular coordinates. [See Eqs. (73)–(75) of [106] for the definition of the WW polarization states and Sec. 8 of [107] for the definition of the B polarization states.] The WW waveforms use the standard definition of GW polarization states, which are the same as those derived from the Weyl scalar, but the B waveforms use an alternate definition; leading to a difference in sign for all the (ℓ, m) modes of h. The angular coordinates in the B waveforms in [107] are derived from circular orbits in the equatorial (xy) plane. To directly compare the NR and

PN waveforms, we must add an inclination to the B waveforms because in the generic case the orbital planes are inclined (with a time dependent inclination angle) with respect to the xy plane. Hence we need to use the procedure developed in [73,108] to transform the (ℓ, m) modes of B waveforms into modes with respect to our rotated spin basis (we provide a simple derivation of these transformations in Appendix A). The following is an outline of the procedure. Let $\vec{L} = \vec{r} \times \vec{p}$ be the instantaneous orbital angular momentum, where

$$\vec{L} = L(\sin\Theta_L \cos\Phi_L, \sin\Theta_L \sin\Phi_L, \cos\Theta_L), \tag{14}$$

$$\vec{r} = r(\sin\Theta_r \cos\Phi_r, \sin\Theta_r \cos\Phi_r, \cos\Theta_r), \tag{15}$$

$$\vec{p} = p(\sin\Theta_p \cos\Phi_p, \sin\Theta_p \cos\Phi_p, \cos\Theta_p), \tag{16}$$

and L, r, p, Θ_L, Φ_L, Θ_r, Φ_r, Θ_p, Φ_p are functions of time. The first step is to rotate the orbital plane onto the xy plane. Let $\mathbf{R}(\alpha, \beta, \gamma)$ be a general rotation defined by the Euler angles α, β, and γ, where we first perform a rotation through angle α about the z axis, followed by a rotation through angle β about the y axis, and finally a rotation through angle γ about the z axis (in practice, we never need to perform this final rotation). Thus a rotation $\mathbf{R}(-\Phi_L(t), -\Theta_L(t), 0)$ transforms $\vec{L}$ and $\vec{r}$ into $\vec{L}'$ and $\vec{r}'$, where

$$\vec{L}' = L(0, 0, 1), \tag{17}$$

$$\vec{r}' = r(\cos\Phi_B(t), \sin\Phi_B(t), 0). \tag{18}$$

The (ℓ, m) modes of the B waveform, in a frame where the orbital plane is the xy plane, can be written in terms of $\cos\Phi_B(t)$, $\sin\Phi_B(t)$, r, and $\omega_{\rm orbit}$. In order to calculate the (ℓ, m) modes of h with respect to the numerical coordinates (where the orbital plane is inclined), we use the results of [73,108]. As was shown in [108], the spin-weighted s spherical harmonics in the numerical coordinates are related to those in the rotated coordinates (where the orbital plane is the xy plane) by

$$Y^s_{\ell m}(\Omega) = e^{is\chi} \sum_{m'} e^{-im'\alpha} K^{\ell s}_{m' m}(-\beta) e^{-im\gamma} Y^s_{\ell m'}(\Omega'), \tag{19}$$

where α, β, and γ are the rotation angles described above (note $\gamma = 0$), and the phase factor $e^{is\chi}$ arises from the transformation of spin-weighted function under a change of spin basis. In [73] it was shown that $K^{\ell s}_{m' m}$ is independent of s (see Appendix A for an alternative proof), and is thus given by [108]

$$K^{\ell s}_{m' m}(-\beta) = d^{\ell}_{m' m}(-\beta), \tag{20}$$

where $d^{\ell}_{m' m}(\beta)$ is the Wigner d matrix given by

$$d^{\ell}_{m' m}(\beta) = \sqrt{(\ell + m)!(\ell - m)!(\ell + m')!(\ell - m')!} \sum_k \frac{(-1)^{k+m'-m}}{k!(\ell + m - k)!(\ell - m' - k)!(m' - m + k)!} \times \left(\sin\frac{\beta}{2}\right)^{2k+m'-m} \left(\cos\frac{\beta}{2}\right)^{2\ell-2k-m'+m}, \tag{21}$$

where the sum over k is such that the factorials are non-negative. Since $h = h' e^{-2i\chi}$, we have

$$h_{\ell m} = \int h \bar{Y}^{-2}_{\ell m} d\Omega = \sum_{m'} \int h' e^{im'\alpha} d^{\ell}_{m' m}(-\beta) h' \bar{Y}^{-2}_{\ell m'}(\Omega') d\Omega' = \sum_{m'} e^{im'\alpha} d^{\ell}_{m' m}(-\beta) h'_{\ell m'} = \sum_{m'} e^{-im'\Phi_L} d^{\ell}_{m' m}(\Theta_L) h'_{\ell m'}. \tag{22}$$

The remaining complication arises from the fact that both the WW and B waveforms contain terms for a nonspinning circular orbit. To avoid adding the common terms twice, we subtract them from the B waveforms. First, using the 1 PN WW formulas, we obtain the waveforms from nonspinning circular orbits in the equatorial plane. We do this by applying the 3 PN EOM for circular orbits to the WW waveform formulas. We then rewrite the waveforms in terms of the gauge invariant variable x, which is the normalized frequency. The B waveforms are given in terms of x, so we can identify those terms in the WW waveforms also present in B waveforms in a unique way. We then remove these terms from the B waveforms. For our generic case, we rotate the subtracted B waveforms modes and add them to the modes of the WW waveforms to obtain the hybrid waveform. Note that there are no significant gauge ambiguities arising from combining the WW and B waveforms in this way because at 1 PN order the harmonic and ADM gauges are equivalent (and hence the WW waveforms are the same in the two gauges) and the B waveforms are given in terms of gauge invariant variables.

Note that we calculate the spin contribution to the waveform through its effect on the orbital motion directly in the WW waveforms and indirectly in B waveforms through the inclination of the orbital plane. Other effects of spin and orbital plane precession on the waveforms are currently not known.

Note that the above procedure for determining the PN waveforms does not contain any arbitrary phase factors or time translations. It was our goal to use a procedure that, given a unique initial configuration, produces a unique waveform. Thus, when comparing the PN and numerical

waveforms we only need to take into account the observer location (i.e. an observers at $100M$ and $200M$ will see waveforms with a time translation of $\sim 100M$ and $\sim 200M$, respectively). To take the observer location into account, we consider the matching of the PN and numerical waveforms over a range of $100M$ in the early part of the waveform (see Sec. IV B 3). We determine the time translation δt in the PN waveform that yields a local maximum in the matching closest to $\delta t = r_{\rm observer}$ (here $r_{\rm observer} = 100M$, which is unrelated to the $100M$ integration time). The observed ambiguities in δt due to gauge effects (both PN and numerical) is of order $5M$ (see Sec. IV B 3).

A. Orbital motion and initial parameters

Following the procedure detailed in [92], extended to spinning particles, we used purely post-Newtonian evolutions of a nearly quasicircular binary with initial orbital separation $r = 50M$ to obtain the positions, momenta, and spins for a noneccentric binary with separation $r \sim 11M$. The idea behind this procedure is that one can specify quasicircular parameters with very low eccentricity for binaries with large separations using the conservative part of the Hamiltonian (i.e. solve for circular orbits). The subsequent PN evolution then provides the PN parameters (including radial momentum) of a closer binary with similar (but lower) eccentricity. The initial quasicircular binary configuration at $r = 50M$ had PN parameters $q = m_1/m_2 = 0.8$, $\vec{S}_1/m_1^2 = (-0.2, -0.14, 0.32)$, and $\vec{S}_2/m_2^2 = (-0.09, 0.48, 0.35)$. We refer to the binary configurations obtained using the truncated 2.5 PN and 3.5 PN EOM as G2.5 and G3.5, respectively. It turns out that the order of the PN evolution is critical for producing low-eccentricity binaries. The eccentricity of the G2.5 configuration, as measured by a subsequent 2.5 PN evolution is quite small. However, both the numerical and 3.5 PN simulations, show that the eccentricity for G2.5 is actually relatively large. Similarly, the eccentricity of the G3.5 configuration, as determined from the full numerical simulation, while smaller than the G2.5 configuration, is still relatively large. We used these $r \sim 11M$ parameters in our numerical and subsequent PN evolutions.

It is interesting to note that in the generic case, the eccentricity, according to 3.5 PN does not decrease with time at smaller radii. To demonstrate this, we show the eccentricity, calculated using the formula $e_r(t) = r^2\ddot{r}/M$, where the magnitude of the oscillations in $e_r(t)$ is the eccentricity. In Fig. 15, we show the eccentricity versus time for a configuration with the same spin magnitudes and mass ratio as our generic case, but with the spins aligned with the orbital angular momentum. As can be seen, the eccentricity decreases with radius. However, in Fig. 16, we show the eccentricity calculated for our configuration, and one slightly modified to give an even lower initial eccentricity, versus time. Here we see that the eccentricity decreases to about $e \sim 0.0005$ and then remains constant. On the other hand, for the low-eccentricity data, the eccentricity actually increases until reaching $e \sim 0.0005$. From the figures is apparent that precession affects induce an apparent ellipticity to the binary's motion that is not radiated away (at least to this order in the PN expansion).

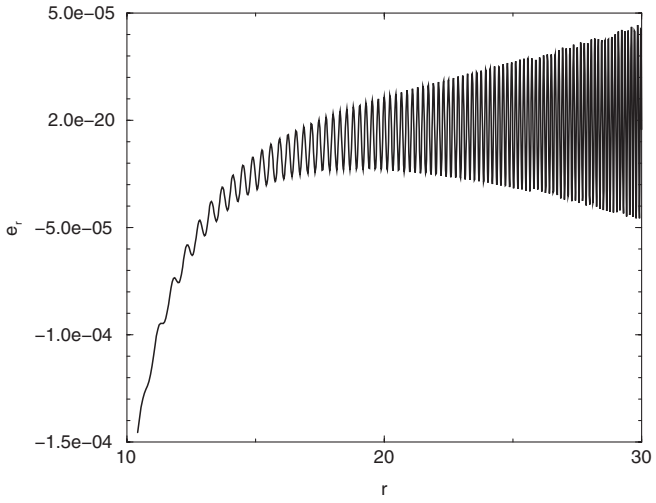

FIG. 15. e_r versus radius for a binary with spins aligned with the angular momentum. Here the eccentricity decreases with r for all radii.

For the G2.5 configuration we used a truncated 2.5 PN evolution, which began at $r = 50M$, to obtain the PN parameters provided in Table IV. The specific spins of the two holes are $S_1/m_1^2 = 0.394\,588\,393\,1$ and $S_2/m_2^2 = 0.600\,832\,755\,4$, respectively. The 2.5 PN ADM mass, $M_{\rm ADM} = m_1 + m_2 + H^R$, for these parameters

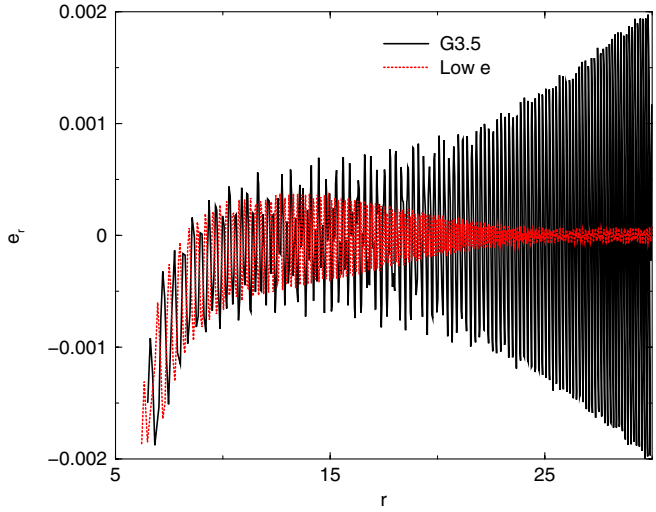

FIG. 16 (color online). e_r versus radius for the G3.5 configuration and a very similar binary, with parameters chosen to reduce the (PN) initial eccentricity. Note that the eccentricity at $r < 10$ is constant and roughly the same for both configurations.

TABLE IV. PN orbital parameters for the G2.5 and G3.5 configuration at an orbital separation of $r \sim 11M$, as calculated directly from PN simulations starting at $r = 50M$. m_1 and m_2 denote the masses, x, y, and z denote the components of $\vec{r} = \vec{x}_1 - \vec{x}_2$, p_i $(i = x, y, z)$ denotes the linear momentum, and S_{1i} and S_{2i} denote the spin angular momenta.

	G2.5	G3.5
m_1/M	0.445 511 564 0	0.445 511 564 0
m_2/M	0.556 889 455 1	0.556 889 455 1
x/M	5.945 345 051 3	−4.597 648 827 1
y/M	−9.208 432 077 0	−9.954 469 474 6
z/M	0.926 094 439 6	−0.877 589 187 3
p_x/M	0.072 376 673 7	0.079 912 054 4
p_y/M	0.047 716 913 1	−0.036 046 899 4
p_z/M	−0.005 371 518 4	−0.000 737 691 38
S_{1x}/M^2	0.017 630 835 7	−0.036 571 185 1
S_{1y}/M^2	0.068 178 851 7	−0.004 966 401 2
S_{1z}/M^2	0.034 271 360 7	0.069 076 853 1
S_{2x}/M^2	−0.065 739 327 8	0.025 637 642 8
S_{2y}/M^2	−0.096 762 497 6	0.148 422 875 9
S_{2z}/M^2	0.145 036 673 6	0.109 697 940 0

is $M_{\rm ADM}/M = 0.992\,568\,273\,6$, where H^R is given by Eq. (12).

When using these parameters in the numerical evolution, and subsequent PN evolutions starting from $r/M_{\rm ADM} = 11.082\,361\,08$, we normalized the PN parameters by the ADM mass (i.e. we use the parameters $\vec{r} \to \vec{r}/M_{\rm ADM}$, $\vec{p} \to \vec{p}/M_{\rm ADM}$, and $\vec{S} \to \vec{S}/M_{\rm ADM}^2$). This renormalization is helpful because we choose to normalize our numerical simulations such that the total ADM mass is 1. However, due to the spurious radiation on the initial slice, the numerical black-hole masses change with time, and eventually equilibrate to a mass ratio of $q = 0.7993$ (the uncertainty in the numerical masses of the two holes was $\delta m \sim 0.000\,03$ at the highest resolutions). Thus in order to compare the PN and numerical waveforms, we need to account for this change in mass ratio. To do this, we modified our choices of m_1 and m_2 such that $M_{\rm ADM}/M = 1$ and $q = m_1/m_2 = 0.7993$. However, because our two PN evolutions systems have different Hamiltonians, we needed to use slightly different values of $m_1/M_{\rm ADM}$ and $m_2/M_{\rm ADM}$ in each case. Note that the spin angular momentum is not affected by the spurious radiation to a significant level because the spurious radiation is nearly axially symmetric about the two holes. For the truncated 2.5 PN evolutions we used

$$\begin{aligned} m_1/M_{\rm ADM} &= 0.448\,627\,492\,8, \\ m_2/M_{\rm ADM} &= 0.561\,275\,482\,1, \end{aligned} \tag{23}$$

i.e. from the equation $M_{\rm ADM} = 1 = (q+1)m_2 + H^R(q, m_2)$, while for the 3.5 PN evolutions we used

$$\begin{aligned} m_1/M_{\rm ADM} &= 0.448\,663\,505\,8, \\ m_2/M_{\rm ADM} &= 0.561\,320\,537\,7, \end{aligned} \tag{24}$$

i.e. $M_{\rm ADM} = 1 = (q+1)m_2 + H^F(q, m_2)$. We verified that these changes in the masses have a negligible effect on the eccentricity and waveforms according to the PN evolutions. We then used both the truncated 2.5 PN and 3.5 PN equations of motion to evolve this modified configuration from $r \approx 11M$. We made one additional change in the truncated 2.5 PN evolution of G2.5. In our original truncated 2.5 PN evolution from $r = 50M$, we used a simpler form of the radiation-reaction term based on PN expansion in the orbital parameters r and $\vec{p}$. While in the subsequent evolution, we used a new expression (consistent with the old expression to 2.5 PN order in the Taylor expansion of the PN orbital parameters) based on an expansion in the orbital frequency [98]. However, because we changed the EOM, the truncated 2.5 PN evolution of the G2.5 configuration, which according to the original system had very low eccentricity, now has a small residual eccentricity (see Fig. 17). The radiation-reaction terms are directly related to the radial motion of the binary. Therefore, the radiation-reaction force is very important to determine the quasicircular configuration, and differences in the force have a strong effect on the motion. This is an indication that 2.5 PN is not accurate enough to model the binary's motion in the $r = 50M$ to $r = 11M$ range.

For the G3.5 configuration, we used a 3.5 PN evolution (that did not include the $H_{S_1S_2,3\,\rm PN}$ term) from $r = 50M$ to

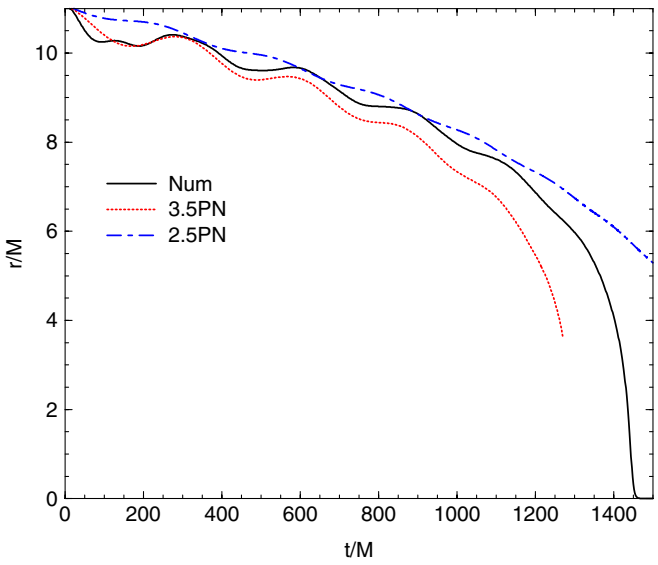

FIG. 17 (color online). The evolution of the orbital radius for the G2.5 configuration from the numerical, 2.5 PN, and 3.5 PN simulations. The residual eccentricity in the 2.5 PN evolution is due to our using a different 2.5 PN radiation-reaction term from that used in the original evolution beginning at $r = 50M$. Note that both 3.5 PN and the numerical simulation indicate that this configuration has relatively large eccentricity.

$r = 11M$ to obtain the orbital parameters provided in Table IV. The 3.5 PN ADM mass of this system is $M_{\rm ADM}/M = 0.9927145092$, and, once again, we renormalized the PN parameters by the ADM mass. When evolving this system numerically, we used slightly altered values of the spin

$$\begin{aligned} S_{1x}/M_{\rm ADM}^2 &= -0.036\,839\,579\,5, \\ S_{1y}/M_{\rm ADM}^2 &= -0.005\,002\,849\,4, \\ S_{1z}/M_{\rm ADM}^2 &= 0.069\,583\,805\,2, \\ S_{2x}/M_{\rm ADM}^2 &= 0.025\,825\,796\,4, \\ S_{2y}/M_{\rm ADM}^2 &= 0.149\,512\,145\,3, \\ S_{2z}/M_{\rm ADM}^2 &= 0.110\,503\,008\,7, \end{aligned} \tag{25}$$

which introduced negligible changes in the waveforms and eccentricity. Here too, we find that the black holes absorb spurious radiation arising from the initial data that changes the mass ratio to 0.799 37. To model this change in the 3.5 PN evolution, we changed the m_1 and m_2 PN masses to $m_1/M_{\rm ADM} = 0.448\,582\,981\,5$ and $m_2/M_{\rm ADM} = 0.561\,170\,648\,8$. Here too, the changes to the masses do not affect the motion or eccentricity of the binary according to the 3.5 PN evolution. Thus, one should use an iterative procedure, like those in Refs. [49,91], to reduce the eccentricity. (We note that the spin of the black holes did not change significantly due to the absorption of the initial burst of radiation. We found that the spin of the smaller black hole changed by $\sim 0.03\%$ and the larger black-hole spin changed by $\sim 0.001\%$ after between $t = 0$ and $t = 25M$. These changes are smaller than the accuracy with which the spin itself can be measured.)

According to the truncated 2.5 PN evolution (with the new radiation-reaction term based on the orbital frequency discussed above), the G2.5 configuration has a relatively small eccentricity, as is apparent in the small oscillations of the time dependence of the 2.5 PN orbital radius displayed in Fig. 17. However, both a subsequent 3.5 PN evolution and the numerical evolution showed that these data were highly eccentric. In Fig. 17, we see that both the 3.5 PN and numerical simulations produce similar, large orbital radius oscillations (which are due to eccentricity). The G3.5 configurations, which has very low eccentricity according to 3.5 PN, as is apparent in the nonoscillatory behavior of the 3.5 PN orbital radius seen in Fig. 18, still shows relatively large oscillations in the orbital radius of the numerical simulation. Thus, using the 3.5 PN equations of motion to generate low-eccentricity initial data reduces the eccentricity, but not nearly to the extent seen in nonspinning binaries [92].

B. Comparison of NR and PN waveforms

We produced both 3.5 PN and 2.5 truncated PN waveforms for the G2.5 configuration and 3.5 PN waveforms for the G3.5 configuration. In Figs. 19 and 20, we show the real part of the ($\ell = 2$, $m = 2$) mode of the strain h for G2.5 and G3.5, respectively. Note the reasonable agreement of the numerical and 3.5 PN waveforms for $700M$ in both configurations. The differences between the PN and numerical waveforms are larger than the numerical waveform

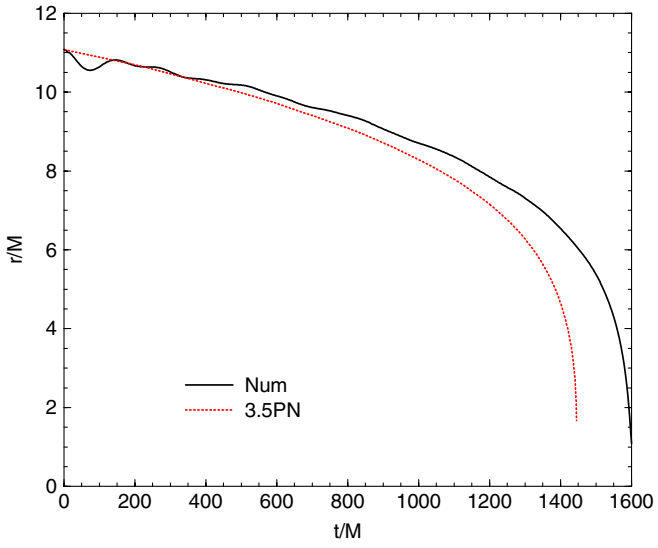

FIG. 18 (color online). The evolutions of the orbital radius for the G3.5 configuration from the numerical and 3.5 PN simulations. Here the numerical simulations shows that the eccentricity was reduced, but is still relatively large, while the 3.5 PN evolution indicates that the binary is noneccentric.

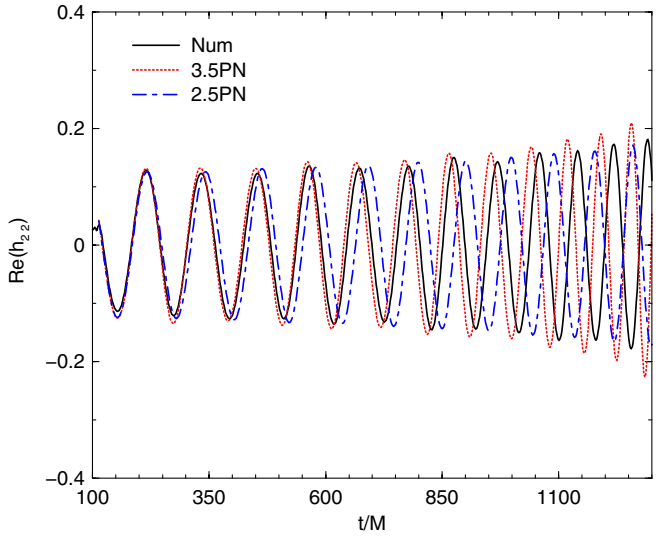

FIG. 19 (color online). The real part of the ($\ell = 2$, $m = 2$) mode of h for the G2.5 configuration from the numerical, truncated 2.5 PN, and 3.5 PN simulations. Note that the 3.5 PN prediction is closer to the numerical waveform and that 3.5 PN predicts an early merger while 2.5 PN predicts a late merger (as is evident by the amplitude of the mode versus time).

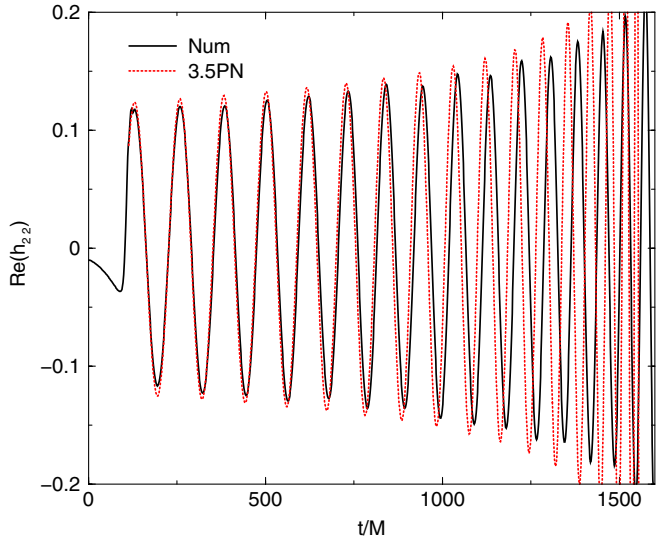

FIG. 20 (color online). The real part of the ($\ell = 2$, $m = 2$) mode of h for the G3.5 configuration from the numerical and 3.5 PN simulations. Here too, 3.5 PN predicts an early merger (as is evident by the amplitude of the mode versus time).

errors at this time. Also note that the 3.5 PN waveform shows evidence of an early merger and has a higher frequency than the numerical waveform, while 2.5 PN waveform shows the opposite behavior. In Figs. 21 and 22, we show the real part of the ($\ell = 2, m = 1$) mode of h for G2.5 and G3.5, respectively. Again, the agreement is fairly good at earlier times and 3.5 PN is more accurate than 2.5 PN. Also, note the interesting oscillatory behavior of the amplitude of the real part of the ($\ell = 2$, $m = 1$) mode for both configurations. Here the amplitude (of the real part) oscillates at about the precessional frequency (see Fig. 14). For the ($\ell = 3$, $m = 3$) mode, we obtained results similar to the ($\ell = 2$, $m = 2$) mode, as seen in Figs. 23 and 24. However, for this mode, oscillations in the amplitude are more pronounced.

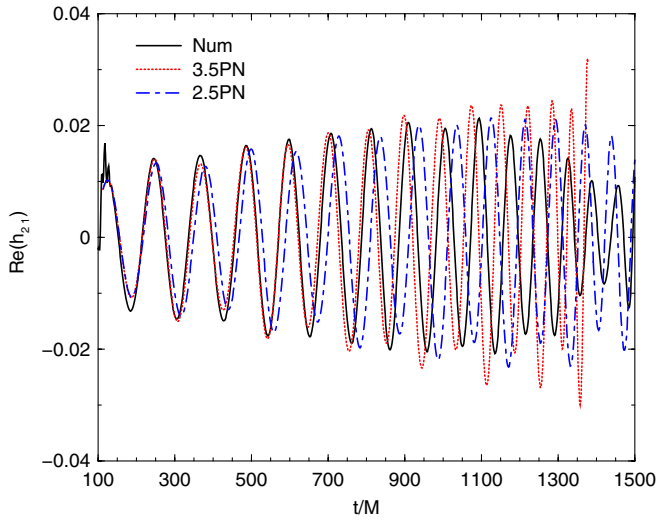

FIG. 21 (color online). The real part of the ($\ell = 2$, $m = 1$) mode of h for the G2.5 configuration from the numerical, truncated 2.5 PN, and 3.5 PN simulations. Note the precession-induced modulation in the amplitude of the oscillations.

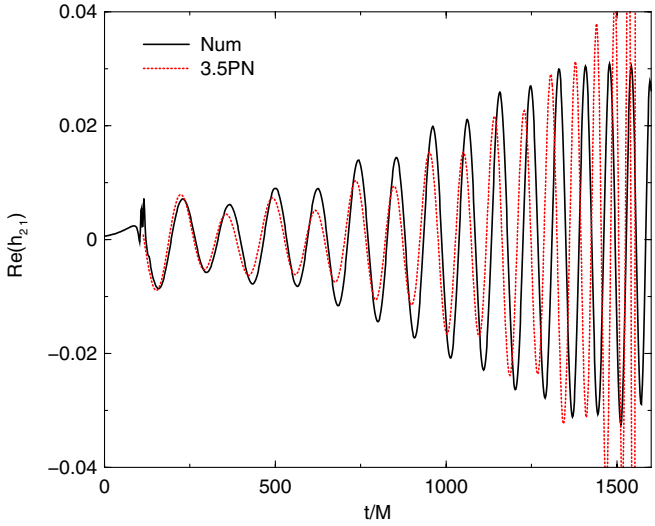

FIG. 22 (color online). The real part of the ($\ell = 2$, $m = 1$) mode of h for the G3.5 configuration from the numerical and 3.5 PN simulations. Note the precession-induced modulation in the amplitude of the oscillations.

1. Amplitudes

We are concerned with exploring two different effects, eccentricity and precession. Long-term precessional effects, which modulate the amplitude of the waveform over many cycles, are more readily apparent in h because

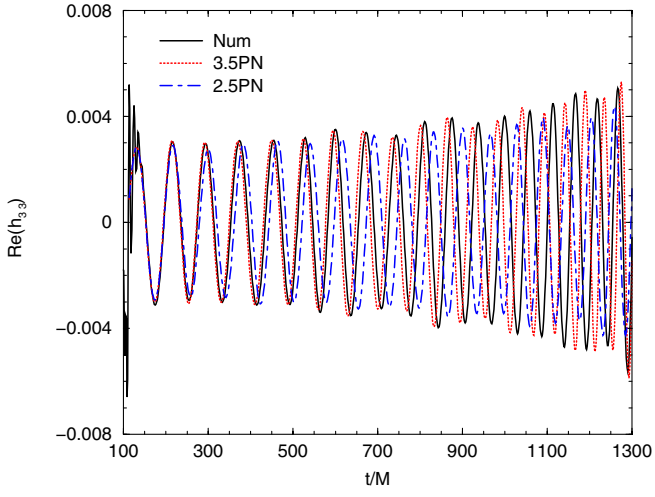

FIG. 23 (color online). The real part of the ($\ell = 3$, $m = 3$) mode of h for the G2.5 configuration from the numerical, truncated 2.5 PN, and 3.5 PN simulations. Note the relatively high-frequency oscillations in the amplitude (roughly corresponding to the orbital period).

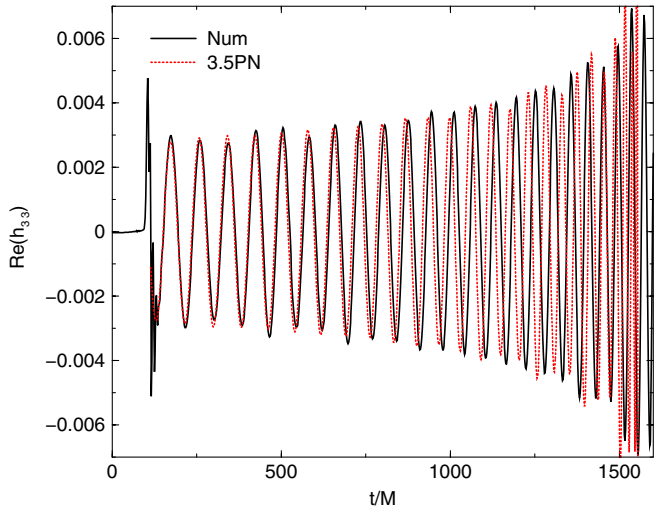

FIG. 24 (color online). The real part of the ($\ell = 3$, $m = 3$) mode of h for the G3.5 configuration from the numerical and 3.5 PN simulations. Note the relatively high-frequency oscillations in the amplitude (roughly corresponding to the orbital period).

differentiating h twice (to obtain ψ_4) suppresses low-frequency oscillations in comparison to higher frequencies. As the binary inspirals, the frequency of the oscillations increases with the orbital frequency. Thus there is a large ramp-up in the amplitude of ψ_4 near merger. This can mask other effects as we observe below. On the other hand, the transformation from ψ_4 to h can induce both high-frequency and low-frequency distortions in h (i.e. numerical errors due to the windowing procedure in the Fourier transform). Thus it is advantageous to compare both ψ_4 and h between the PN and numerical simulations. Here we calculate the post-Newtonian (ℓ, m) modes of $\psi_4(t)$ by taking two time derivatives of the (ℓ, m) modes of $h(t)$.

In order to analyze the behavior of the (ℓ, m) modes of the waveform, we decompose the modes into amplitudes and phases. In Fig. 25, we show the amplitude of the ($\ell = 2$, $m = 2$) mode of h for the G2.5 configuration. Here the 2.5 PN waveforms appear to capture the overall amplitude behavior to better accuracy, while the 3.5 PN waveforms capture the oscillations in the amplitude. These oscillations occur at roughly the orbital frequency and are due mainly to eccentricity and, to a lesser extent, precession. As discussed above, precession can induce an oscillation in the ($\ell = 2$, $m = 2$) mode at the orbital frequency by mixing the ($\ell = 2$, $m = 2$) and ($\ell = 2$, $m = \pm 1$) modes (and since the m modes have frequency $\sim |m|\omega_{\rm orbit}$, where $\omega_{\rm orbit}$ is the orbital frequency, the resulting modes will show a beating effect at the orbital frequency). A similar plot for the G3.5 configuration, Fig. 26, shows that 3.5 PN predicts very small amplitude oscillations, which seem to confirm that the oscillations seen in G2.5 are mainly due to eccentricity. Note that in Fig. 26 the amplitude of the numerical ($\ell = 2$, $m = 2$) mode oscillates at about the orbital frequency with a significantly larger amplitude than the 3.5 PN prediction; indicating that these oscillations are due to eccentricity (which is consistent with the relatively large oscillations in the numerical orbital radius). Since the transformation from ψ_4 to h can induce artifacts into the waveforms, it is also important to compare the PN predictions for ψ_4 with the numerical waveforms. In Figs. 27 and 28, we show the amplitude of the ($\ell = 2$,

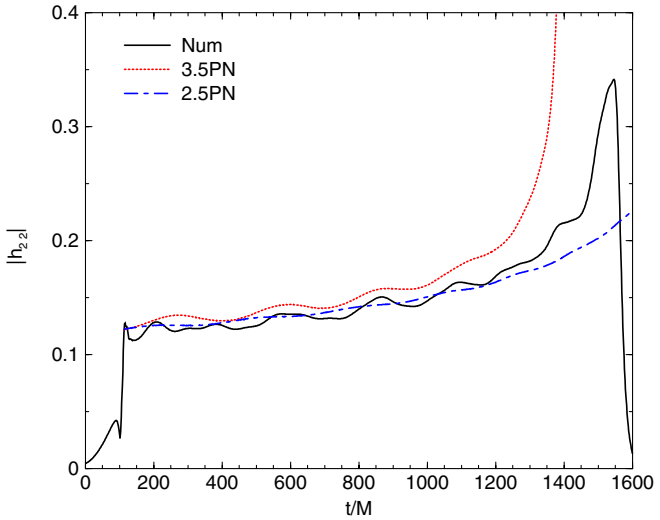

FIG. 25 (color online). The amplitude of the ($\ell = 2$, $m = 2$) mode of h for the G2.5 configuration from the numerical, truncated 2.5 PN, and 3.5 PN simulations. The oscillations in the amplitude are much more pronounced in the numerical and 3.5 PN simulations, indicating that these oscillations are likely due to eccentricity.

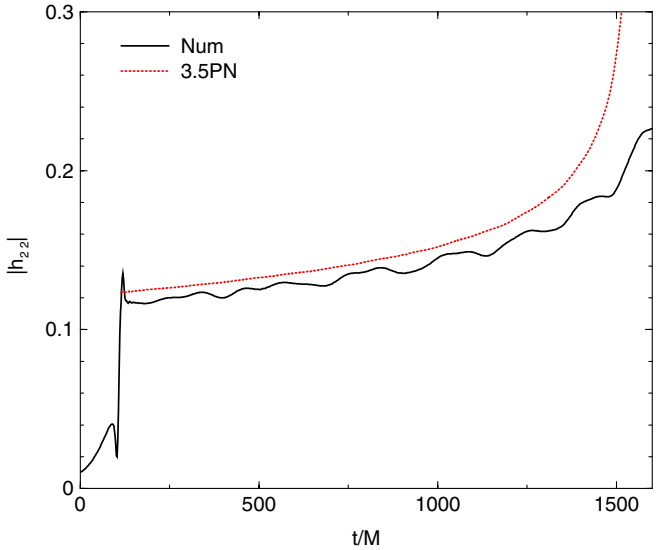

FIG. 26 (color online). The amplitude of the ($\ell = 2$, $m = 2$) mode of h for the G3.5 configuration from the numerical and 3.5 PN simulations. The amplitude oscillations in the numerical waveform are much larger than those in the 3.5 PN waveform, indicating that they are likely due to eccentricity.

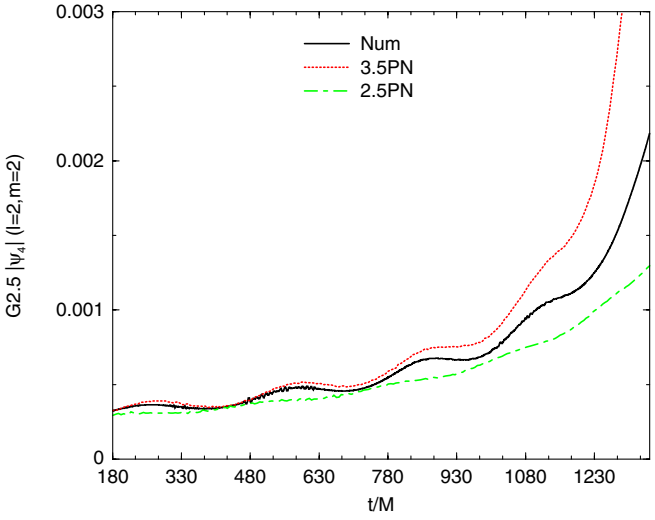

FIG. 27 (color online). The amplitude of the ($\ell = 2$, $m = 2$) mode of ψ_4 for the G2.5 configuration from the numerical, truncated 2.5 PN, and 3.5 PN simulations. Note the very good agreement between the 3.5 PN and numerical waveforms.

$m = 2$) of ψ_4 for the G2.5 and G3.5 configurations, respectively. Note that, for ψ_4, 3.5 PN gives a clearly better fit to the G2.5 waveform than truncated 2.5 PN. Note also that the agreement between the 3.5 PN and numerical ψ_4 appears to be significantly better than the agreement in h. Thus it appears that the windowing procedure has induced a very low-frequency mode into h that yielded a net change in the amplitude of the waveform.

The effects of precession become apparent in the subleading modes h (and to a lesser extent, in the subleading modes of ψ_4). However, numerical errors in the lower amplitude modes are also more pronounced. In Fig. 29 and 30 we show the amplitudes of the ($\ell = 2$, $m = 1$)

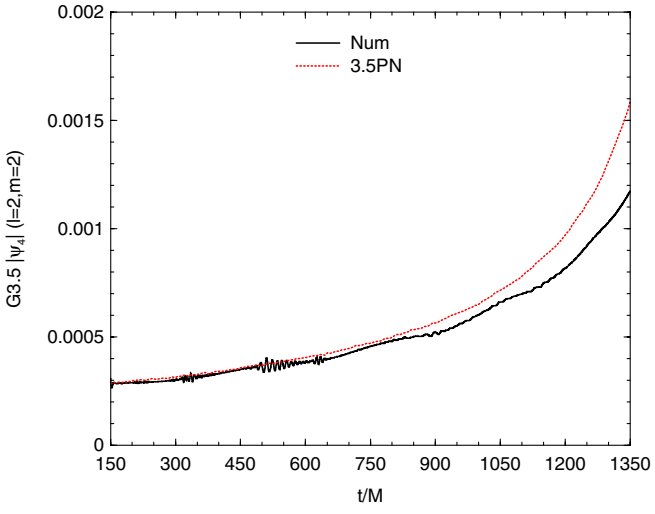

FIG. 28 (color online). The amplitude of the ($\ell = 2$, $m = 2$) mode of ψ_4 for the G3.5 configuration from the numerical and 3.5 PN simulations.

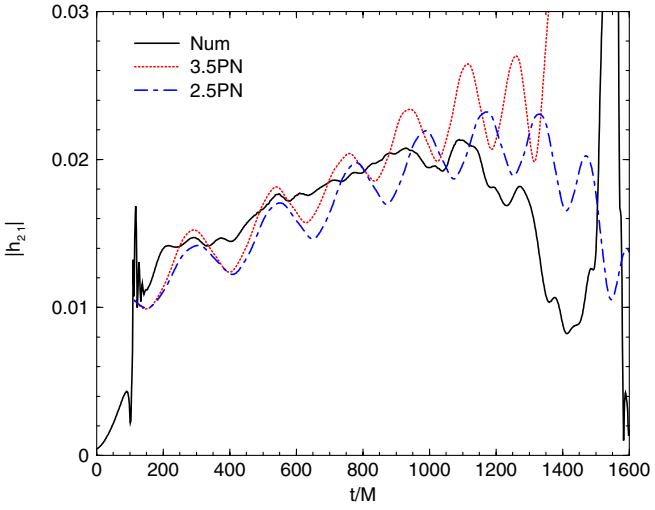

FIG. 29 (color online). The amplitude of the ($\ell = 2$, $m = 1$) mode of h for the G2.5 configuration from the numerical, truncated 2.5 PN, and 3.5 PN simulations. The secular oscillation in the numerical amplitude occurs at roughly the precessional frequency. Here the shorter time scale oscillations apparent in the PN waveforms are much smaller in the numerical waveform.

mode of h for the G2.5 and G3.5 configurations, respectively. Here both 2.5 PN and 3.5 PN capture the secular behavior in the amplitude nicely. Unlike for the ($\ell = 2$, $m = 2$) mode, here the PN amplitudes oscillate much more strongly than the numerical amplitudes for the G2.5 configuration, while 3.5 PN seems to capture both the short (orbital frequency) time scale oscillations and the longer

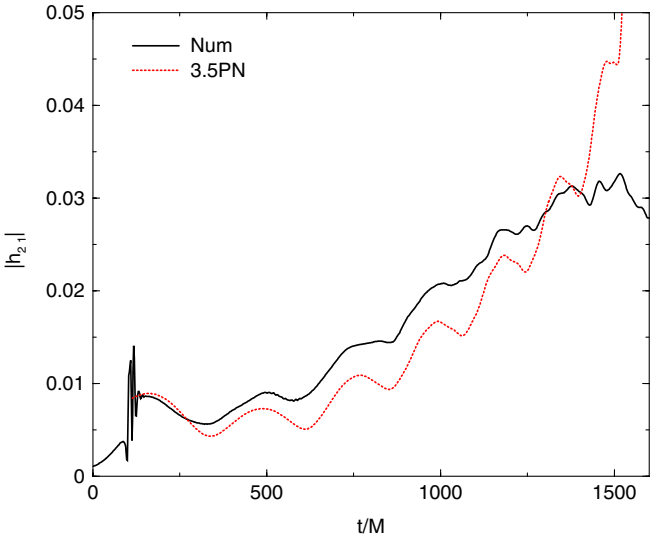

FIG. 30 (color online). The amplitude of the ($\ell = 2$, $m = 1$) mode of h for the G3.5 configuration from the numerical and 3.5 PN simulations. The secular oscillation in the numerical amplitude occurs at roughly the precessional frequency. Here the shorter time scale oscillations (corresponding roughly to the orbital period) are present in both waveforms with very similar amplitudes.

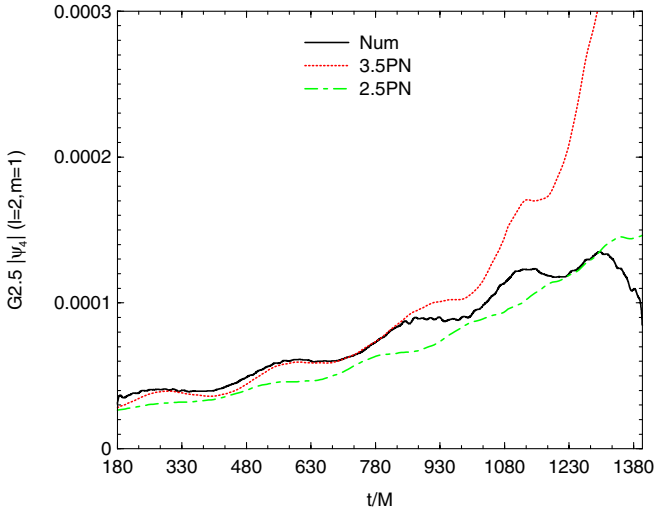

FIG. 31 (color online). The amplitude of the ($\ell = 2$, $m = 1$) mode of ψ_4 for the G2.5 configuration from the numerical, truncated 2.5 PN, and 3.5 PN simulations. Note the very good agreement between the 3.5 PN and numerical waveforms.

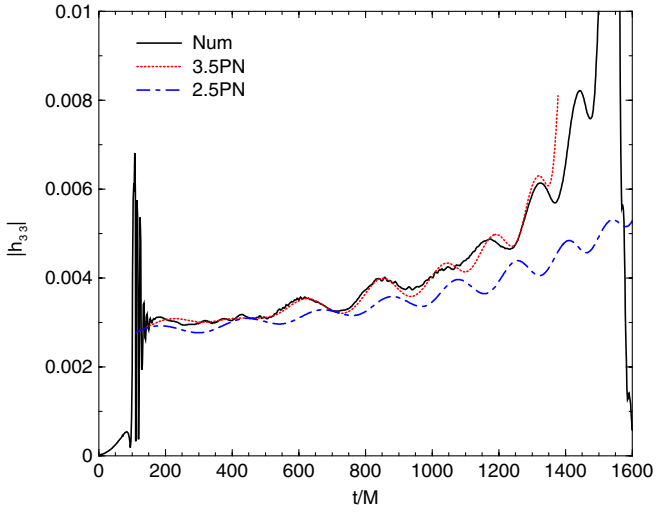

FIG. 33 (color online). The amplitude of the ($\ell = 3$, $m = 3$) mode of h for the G2.5 configuration from the numerical, truncated 2.5 PN, and 3.5 PN simulations. Note the very good agreement between the 3.5 PN and numerical waveforms. Also note that the short time scale oscillations (orbital period) grow with time at later times, indicating that, at least at later times, they are due mainly to precession.

(precessional) frequency oscillation (until $t \sim 1000M$) for the G3.5 configuration. The damping of the numerical oscillations for the G2.5 configuration are likely a consequence of the windowing procedure (which acts as a high-frequency and low-frequency filter), as a similar damping is not apparent in ψ_4 (see Figs. 30 and 32). Although the G3.5 configuration has very low eccentricity (according to 3.5 PN), the effects of eccentricity can increase as the binary separation falls below $15M$ (see Fig. 16). This effect appears to be related to precession because the eccentricity of nonprecessing binaries (see Fig. 15) decreases uniformly with binary separation. In addition, mode-mixing effects may also be partially responsible for these oscillations in the amplitude of the ($\ell = 2$, $m = 1$) mode at the orbital frequency. The secular oscillation in the amplitude of the ($\ell = 2$, $m = 1$) mode matches the precessional frequency (see Figs. 13 and 30), and is thus likely a direct consequence of precession [the amplitude of the ($\ell = 2$, $m = 1$) mode contains significant contributions from the spins; see Eq. (3) in [109]].

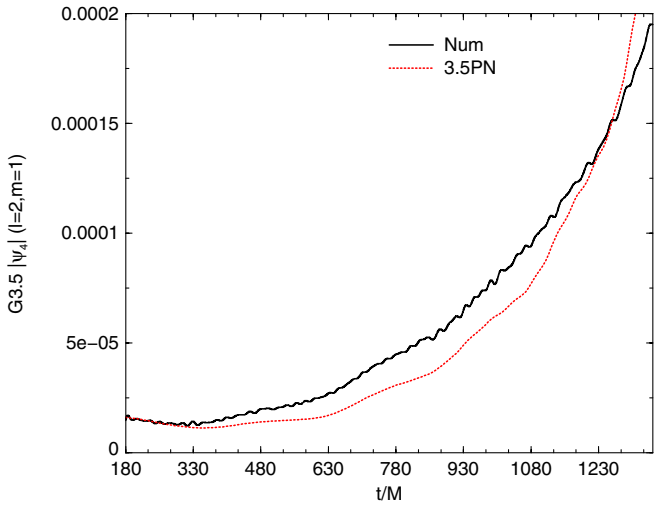

FIG. 32 (color online). The amplitude of the ($\ell = 2$, $m = 1$) mode of ψ_4 for the G3.5 configuration from the numerical and 3.5 PN simulations.

The ($\ell = 2$, $m = 1$) mode of ψ_4, as seen in Figs. 31 and 32 again shows that the 3.5 PN waveforms are clearly more accurate than the truncated 2.5 PN waveforms. The agreement of the 3.5 PN waveforms for the G2.5 configuration is remarkable. Note that the long time scale oscillation seen in the ($\ell = 2$, $m = 1$) mode of h, which is likely due to precession, is not apparent in ψ_4 of the G3.5 configuration. However, as this effect is smaller in G3.5 (as seen by comparing Figs. 31 and 32), it may be hidden in ψ_4 by the ramp-up in amplitude of ψ_4 near merger.

Finally, in Fig. 33 and 34, we show the amplitudes of the ($\ell = 3$, $m = 3$) mode of h for the G2.5 and G3.5 configurations, respectively. An interesting feature of these modes is that the late-time amplitude oscillations, which are roughly at the orbital frequency, increase with time, indicating that they are due to the precession-induced late-time eccentricity apparent in Fig. 16. For the G2.5 configuration, 3.5 PN produces a remarkably good fit, capturing all oscillations in the amplitude until $t \sim 1400M$. On the other hand, 3.5 PN does not capture the early-time oscillations in the G3.5 configuration. A possible explanation for this result is that, as seen in Figs. 17 and 18, both 3.5 PN and the numerical simulation show similar eccentricities for the G2.5 configuration, but 3.5 PN shows much lower eccen-

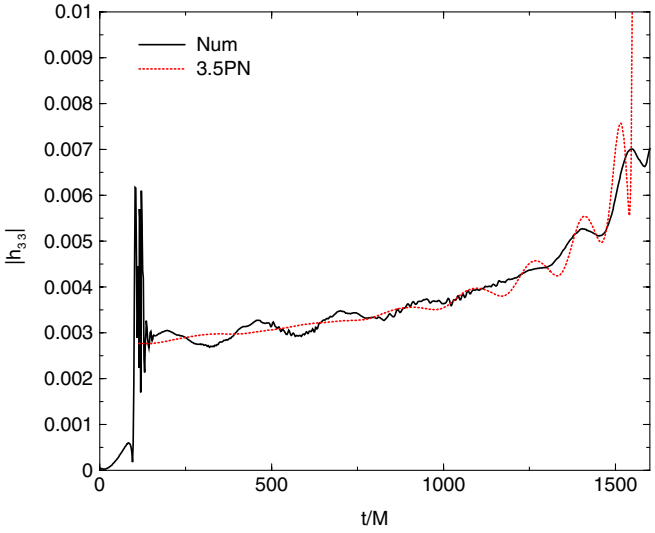

FIG. 34 (color online). The amplitude of the ($\ell = 3$, $m = 3$) mode of h for the G3.5 configuration from the numerical and 3.5 PN simulations. Note that the short time scale oscillation at later times grow with time, indicating that these later-time oscillations are due to precession. The early-time oscillations in the numerical waveform (at the same frequency) are likely due to eccentricity.

tricity for the G3.5 configuration. This eccentricity leads to the early-time oscillation in the amplitude of the ($\ell = 3$, $m = 3$) mode that are not captured by 3.5 PN. However, as the binary evolves, the effects of precession-induced eccentricity in the PN EOM increase and eventually dominate. This causes the amplitude of the oscillations in the 3.5 PN waveform to increase and eventually become larger than the numerical amplitude oscillations. In Figs. 35 and 36, we show the amplitude of the ($\ell = 3$, $m = 3$) mode of

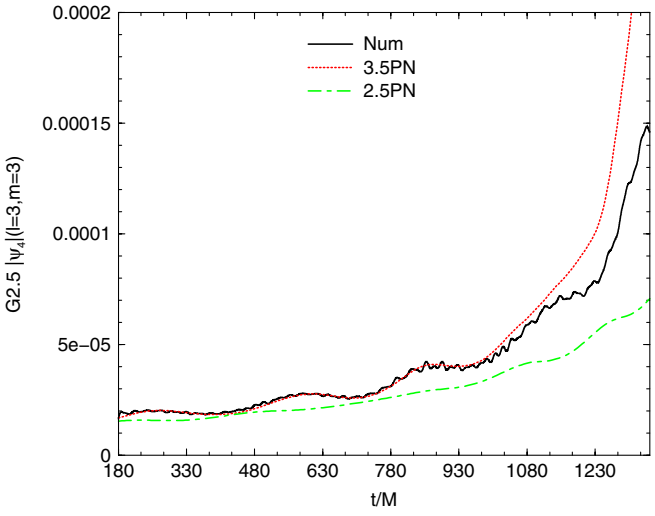

FIG. 35 (color online). The amplitude of the ($\ell = 3$, $m = 3$) mode of ψ_4 for the G2.5 configuration from the numerical, truncated 2.5 PN, and 3.5 PN simulations. Note the very good agreement between the 3.5 PN and numerical waveforms.

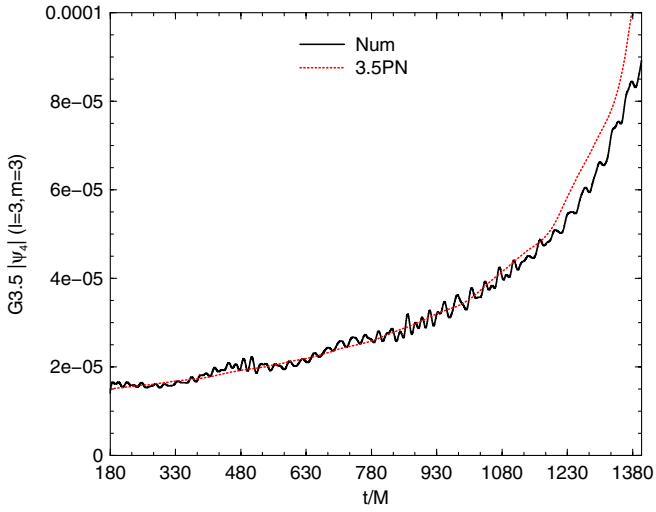

FIG. 36 (color online). The amplitude of the ($\ell = 3$, $m = 3$) mode of ψ_4 for the G3.5 configuration from the numerical and 3.5 PN simulations.

ψ_4 for the G2.5 and G3.5 configurations. Here too 3.5 PN gives a remarkably good estimation for the amplitude of the mode. Note that the orbital-frequency oscillations seen in Fig. 34 are not readily apparent in Fig. 36 (even in the PN waveforms). This shows one advantage of analyzing h over ψ_4; eccentricity and precessional effects are more apparent in h.

From the amplitudes of each mode, we see that precession and eccentricity impart signatures on the modes of the waveform at the orbital frequency. However, the long-time oscillations in the amplitudes, here apparent only in the ($\ell = 2$, $m = \pm 1$) modes, seem to be due purely to precession, and occur at the precessional frequency.

2. Phases

In Figs. 37 and 38, we show the phase differences between the 3.5 PN and numerical waveforms for the ($\ell = 2$, $m = 1$), ($\ell = 2$, $m = 2$), and ($\ell = 3$, $m = 3$) modes. Note that we calculate the phase of the PN and numerical waveforms directly from the appropriate (ℓ, m) mode and do not add any additional phase factors (see Sec. IV). In all cases we normalized the phase differences by dividing by $\ell\pi$. Note that we renormalize by $\ell\pi$, rather than $m\pi$. If the orbital plane were to lie along the xy plane, or equivalently, we chose spherical coordinates such that the $\theta = 0$ corresponds to direction of normal to the orbital plane, then we would expect the (ℓ, m) modes to have frequency $\omega \approx m\omega_{\rm orbit}$, and an error in the orbital phase of $\delta\Phi_{\rm orbit}$ would lead to an error in the phase of the (ℓ, m) modes of $m\delta\Phi_{\rm orbit}$. However, in that case the ($\ell = 2$, $m = 1$) mode would be very small. Consequently, in our nonaligned spin basis, the ($\ell = 2$, $m = 1$) mode is actually dominated by contributions from the ($\ell = 2$, $m = \pm 2$) modes (of the aligned spin basis). Thus, in our configurations, the

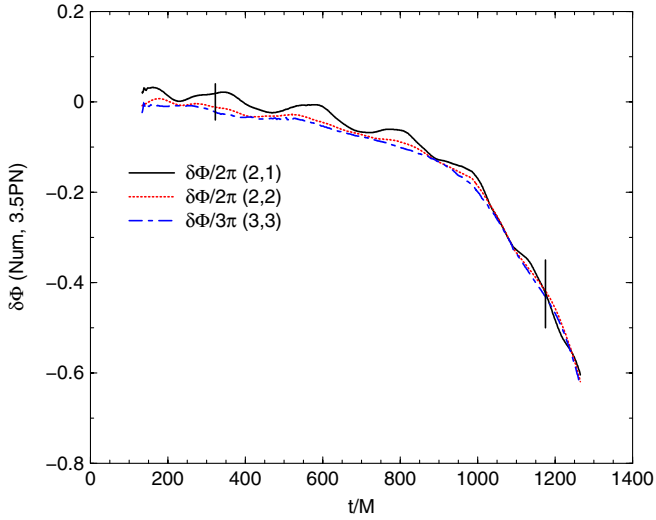

FIG. 37 (color online). The phase differences in h between the numerical and 3.5 PN simulations for the G2.5 configuration in the ($\ell = 2$, $m = 1$), ($\ell = 2$, $m = 2$), and ($\ell = 3$, $m = 3$) modes. We multiplied the phase differences in the modes by a factor of $1/(\ell\pi)$. We divide by $\ell\pi$, rather than $m\pi$, because the ($\ell = 2$, $m = 1$) mode is dominated by mode mixing from the ($\ell = 2$, $m = \pm 2$) modes (see text for more details). The vertical lines shows the times when the ($\ell = 2$, $m = 2$) frequency is $M\omega = 0.05$ ($t \sim 323M$) and $M\omega = 0.075$ ($t \sim 1075M$).

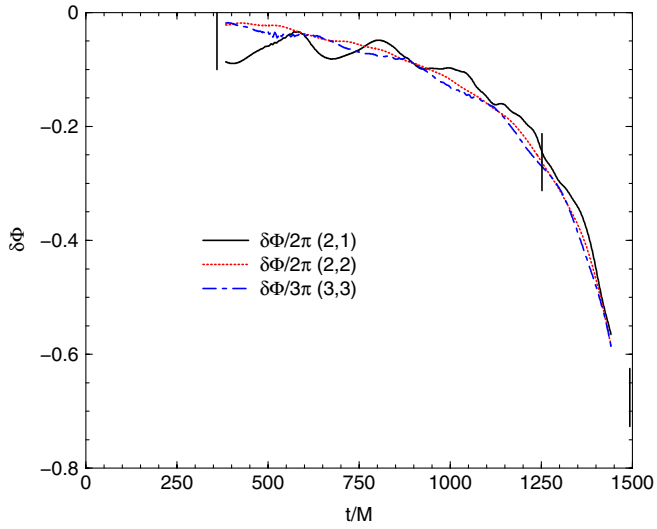

FIG. 38 (color online). The phase differences in h between the numerical and 3.5 PN simulations for the G3.5 configuration in the ($\ell = 2$, $m = 1$), ($\ell = 2$, $m = 2$), and ($\ell = 3$, $m = 3$) modes. We multiplied the phase differences in the modes by a factor of $1/(\ell\pi)$. Note that the normalized phase differences are qualitatively independent of the mode and arise from the orbital phase error in the PN approximation. We divide by $\ell\pi$, rather than $m\pi$, because the ($\ell = 2$, $m = 1$) mode is dominated by mode mixing from the ($\ell = 2$, $m = \pm 2$) modes (see text for more details). The vertical lines show the times when the ($\ell = 2$, $m = 2$) frequency is $M\omega = 0.05$ ($t \sim 360M$), $M\omega = 0.075$ ($t \sim 1252M$), and $M\omega = 0.1$ ($t \sim 1493M$).

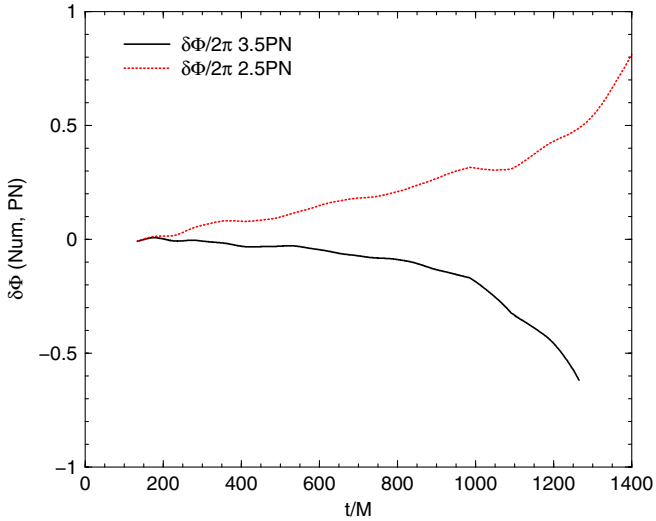

FIG. 39 (color online). The phase difference in the ($\ell = 2$, $m - 2$) mode of h between the NR and PN waveforms for the G2.5 configuration. The vertical axis denotes the number of orbital rotations derived from GW cycle. Note that the normalized phase differences are qualitatively independent of the mode and arise from the orbital phase error in the PN approximation.

($\ell = 2, m = 1$) mode has frequency $2\omega_{\rm orbit}$ and the error in the phase scales like $2\delta\Phi_{\rm orbit}$. Note that the renormalized phase differences are qualitatively independent of the mode. We therefore focus on the ($\ell = 2$, $m = 2$) mode. In Fig. 39, we show the phase difference between the numerical, 2.5 PN, and 3.5 PN ($\ell = 2$, $m = 2$) mode of h for the G2.5 configuration. From the plot we see that the phase difference improves with the higher PN order and changes sign. It thus appears that still higher-order PN corrections may make the waveform phases agree. As seen in Figs. 19, 21, and 23, the truncated 2.5 PN phase evolution is slower than that of the NR and 3.5 PN, and thus its phase lags behind the other two. The 3.5 PN evolution merges too quickly (but is still closer to the numerical evolution) and thus its phase leads the numerical one.

3. Matching

In order to quantitatively compare the modes of the truncated 2.5 PN and 3.5 PN waveforms with the numerical waveforms we define the overlap, or matching criterion, for the real and imaginary parts of each mode as

$$M^{\Re}_{\ell m} = \frac{\langle R^{\rm Num}_{\ell m}, R^{\rm PN}_{\ell m}\rangle}{\sqrt{\langle R^{\rm Num}_{\ell m}, R^{\rm Num}_{\ell m}\rangle\langle R^{\rm PN}_{\ell m}, R^{\rm PN}_{\ell m}\rangle}}, \tag{26}$$

$$M^{\Im}_{\ell m} = \frac{\langle I^{\rm Num}_{\ell m}, I^{\rm PN}_{\ell m}\rangle}{\sqrt{\langle I^{\rm Num}_{\ell m}, I^{\rm Num}_{\ell m}\rangle\langle I^{\rm PN}_{\ell m}, I^{\rm PN}_{\ell m}\rangle}}, \tag{27}$$

where $R_{\ell m} = {\rm Re}(h_{\ell m})$, $I_{\ell m} = {\rm Im}(h_{\ell m})$, and

$$\langle f, g\rangle = \int_{t_1}^{t_2} f(t)g(t)dt. \quad (28)$$

Hence, $M^{\Re}_{\ell m} = M^{\Im}_{\ell m} = 1$ indicates that the given PN and numerical mode agree. To compare PN and numerical waveforms, we need to determine the time translation δt between the numerical time and the corresponding point on the PN trajectory. That is to say, the time it takes for the signal to reach the extraction sphere (here $r = 100M$). We determine this time translation by finding the time translation near $\delta t = 100M$ that maximizes the agreement of the early-time waveforms in the ($\ell = 2$, $m = \pm 2$), ($\ell = 2$, $m = \pm 1$), and ($\ell = 3$, $m = \pm 3$) simultaneously (in practice we look at the matching over the first $100M$ after the spurious radiation has left the system). We find $\delta t \sim 112$, in good agreement with the expectation for our observer at $r = 100M$. We also determine an alternate time translation, one full wavelength in the ($\ell = 2$, $m = 2$) mode longer, that increases the matching of the ($\ell = 2$, $m = 2$) mode over longer integration periods. On the other hand, this new time translation, $\delta t = 233$, causes the ($\ell = 3$) modes to be out of phase, leading to negative overlaps. Thus by looking at the ($\ell = 2$) and ($\ell = 3$) modes simultaneously, we can reject this false match. The results of these matching studies are summarized in Tables V and VI.

TABLE V. The overlap (matching) of the real and imaginary parts of the modes of h of the G2.5 configuration for the truncated 2.5 PN and 3.5 PN waveforms and the numerical waveforms for various integration times and PN time translation δt. In all cases, we start the integration just after the numerical initial data (spurious radiation) pulse leaves the system.

Integration Time	600	800	1000
Truncated 2.5 PN ($\delta t = 112.2$)			
Re ($\ell = 2$, $m = 2$)	0.789	0.615	0.365
Re ($\ell = 2$, $m = 1$)	0.705	0.501	0.292
Re ($\ell = 3$, $m = 3$)	0.596	0.286	−0.038
3.5 PN ($\delta t = 112.2$)			
Re ($\ell = 2$, $m = 2$)	0.975	0.922	0.693
Im ($\ell = 2$, $m = 2$)	0.976	0.924	0.723
Re ($\ell = 2$, $m = -2$)	0.975	0.922	0.693
Im ($\ell = 2$, $m = -2$)	0.978	0.926	0.723
Re ($\ell = 2$, $m = 1$)	0.982	0.938	0.687
Im ($\ell = 2$, $m = 1$)	0.977	0.924	0.699
Re ($\ell = 2$, $m = -1$)	0.984	0.939	0.707
Im ($\ell = 2$, $m = -1$)	0.980	0.933	0.711
Re ($\ell = 3$, $m = 3$)	0.908	0.794	0.418
Im ($\ell = 3$, $m = 3$)	0.916	0.795	0.435
Re ($\ell = 3$, $m = -3$)	0.909	0.782	0.403
Im ($\ell = 3$, $m = -3$)	0.912	0.794	0.426
3.5 PN ($\delta t = 233.3$)			
Re ($\ell = 2$, $m = 2$)	0.928	0.803	0.746
Re ($\ell = 2$, $m = 1$)	0.918	0.800	0.774
Re ($\ell = 3$, $m = 3$)	−0.850	−0.602	−0.492

TABLE VI. The overlap of the real and imaginary parts of the modes of h of the G3.5 configuration for the 3.5 PN waveforms and the numerical waveforms. In all cases, we start the integration just after the numerical initial data (junk radiation) pulse leaves the system.

Integration Time	600	800	1000
3.5 PN ($\delta t = 112.5$)			
Re ($\ell = 2$, $m = 2$)	0.986	0.964	0.895
Im ($\ell = 2$, $m = 2$)	0.987	0.962	0.900
Re ($\ell = 2$, $m = -2$)	0.986	0.964	0.895
Im ($\ell = 2$, $m = -2$)	0.987	0.962	0.901
Re ($\ell = 2$, $m = 1$)	0.904	0.912	0.843
Im ($\ell = 2$, $m = 1$)	0.916	0.901	0.820
Re ($\ell = 2$, $m = -1$)	0.920	0.908	0.833
Im ($\ell = 2$, $m = -1$)	0.917	0.903	0.816
Re ($\ell = 3$, $m = 3$)	0.938	0.891	0.738
Im ($\ell = 3$, $m = 3$)	0.919	0.868	0.721
Re ($\ell = 3$, $m = -3$)	0.931	0.880	0.733
Im ($\ell = 3$, $m = -3$)	0.906	0.857	0.721

As seen in the tables, the matching of the 3.5 PN and numerical waveforms are significantly better than the matching of the 2.5 PN and numerical waveforms for all modes. Similarly, all PN modes match the numerical waveforms better over the shorter integration times. This is consistent with the qualitative agreements in the waveforms seen in Figs. 19–24. Note that the 3.5 PN and numerical waveform matches for all modes are significantly better for the G3.5 configuration than the G2.5

TABLE VII. The overlap (matching) of the real and imaginary parts of the modes of ψ_4 of the G2.5 configuration for the truncated 2.5 PN and 3.5 PN waveforms and the numerical waveforms for various integration times with the PN time translation $\delta t = 106.5$ for the truncated 2.5 PN and $\delta t = 113.0$ for the 3.5 PN. In all cases, we start the integration after $t = 180$. The integration time means that the end of integration is the same as that used in the overlap of h.

Integration Time	600	800	1000
Truncated 2.5 PN ($\delta t = 106.5$)			
Re ($\ell = 2$, $m = 2$)	0.900	0.744	0.435
Im ($\ell = 2$, $m = 2$)	0.898	0.717	0.469
Re ($\ell = 2$, $m = 1$)	0.824	0.654	0.408
Im ($\ell = 2$, $m = 1$)	0.851	0.675	0.431
Re ($\ell = 3$, $m = 3$)	0.767	0.472	0.00578
Im ($\ell = 3$, $m = 3$)	0.776	0.477	0.0102
3.5 PN ($\delta t = 113.0$)			
Re ($\ell = 2$, $m = 2$)	0.980	0.909	0.519
Im ($\ell = 2$, $m = 2$)	0.984	0.916	0.563
Re ($\ell = 2$, $m = 1$)	0.982	0.936	0.544
Im ($\ell = 2$, $m = 1$)	0.976	0.921	0.594
Re ($\ell = 3$, $m = 3$)	0.906	0.759	0.150
Im ($\ell = 3$, $m = 3$)	0.906	0.754	0.140

TABLE VIII. The overlap of the real and imaginary parts of the modes of ψ_4 of the G3.5 configuration for the 3.5 PN waveforms and the numerical waveforms with $\delta t = 113.5$. In all cases, we start the integration after $t = 180$. The integration time means that the end of integration is the same as that used in the overlap of h.

Integration Time	600	800	1000
3.5 PN ($\delta t = 113.5$)			
Re ($\ell = 2$, $m = 2$)	0.981	0.962	0.860
Im ($\ell = 2$, $m = 2$)	0.983	0.958	0.876
Re ($\ell = 2$, $m = 1$)	0.882	0.927	0.850
Im ($\ell = 2$, $m = 1$)	0.853	0.893	0.811
Re ($\ell = 3$, $m = 3$)	0.869	0.841	0.640
Im ($\ell = 3$, $m = 3$)	0.868	0.834	0.649

configuration for the longer $t = 1000M$ integration time [the differences between the matches are most striking for ($\ell = 3$, $m = \pm 3$) modes, where the matching is $\sim$0.7 for G3.5 and $\sim$0.4 for G2.5]. The only place where the matches for the G2.5 configuration are consistently better than the matches for the G3.5 configuration is the is the ($\ell = 2$, $m = \pm 1$) modes for the shorter integration times. Thus, it appears that the 3.5 PN waveforms, in general, produce superior results for the more circular G3.5 configuration, which is likely due to the fact that the higher PN order B waveforms are accurate for quasicircular, rather than eccentric, binaries.

In Tables VII and VIII we show the matching of the modes of ψ_4 between 2.5 PN, 3.5 PN, and the numerical ψ_4. Here we find a better match when we use a slightly altered time offset. Note that matching is generally worse than that observed with h, especially for the longer integration times. This is consistent with the observation that the amplitude of ψ_4 increases more rapidly in time than h (due to the effects of increasing frequency and the two time derivatives). Thus a matching of ψ_4 emphasizes the disagreement between the PN and numerical waveforms at later times. Interestingly, the matching in G3.5 is significantly better than G2.5 for the $1000M$ integration time, particularly in the ($\ell = 3$, $m = 3$) mode, where the matching between the 3.5 PN and numerical ψ_4 is 65% for G3.5 and only 14% for G2.5.

V. CONCLUSION

We analyzed the first long-term generic waveform produced by the merger of unequal mass, unequal spins, precessing black-hole binaries (a shorter simulation of this kind, which led to the discovery of the very large recoil configuration, was reported in [15]). We demonstrated eighth-order convergence of the waveform phase and fourth-order convergence of the amplitude (consistent with the order of accuracy of the extraction routine) in the numerical results. These waveforms clearly show the effects of eccentricity and precession on the amplitude in the subleading ($\ell = 2$, $m = 1$) and ($\ell = 3$, $m = 3$) modes. In particular, analyzing the ($\ell = 2$, $m = 1$) mode provides a way of detecting precessional effects in the observed waveforms. We have also found that there are two sources of eccentricity for a generic binary. Residual eccentricity, due to a nonideal choice of initial data parameters that tends to damp out as the binary separation decreases, and precession-induced eccentricity that grows as the orbital separation falls below $\sim 15M$ (this increase in eccentricity at later times is apparent in the ($\ell = 3$, $m = 3$) mode of h in both the PN and numerical waveforms).

We have compared these waveforms with the truncated 2.5 post-Newtonian waveforms, as well as the waveforms with the nonspinning 3.0 PN conservative and 3.5 PN radiative corrections. We find a good initial agreement of waveforms for the first six cycles, with overlaps of over 97% for the ($\ell = 2$, $m = \pm 2$) modes, 90%–98% for the ($\ell = 2$, $m = \pm 1$), and over 90% for the ($\ell = 3$, $m = \pm 3$) modes. This provides a natural way to match numerical waveforms to the post-Newtonian ones with a time translation (the same for all modes) motivated by the physical location of the observer (see Fig. 20, for instance). The agreement degrades as we approach the more dynamical region of the late merger and plunge. The disagreement begins in a region where the numerical waveform is still very accurate. Thus it appears that the disagreement is mainly due to errors introduced by truncating the PN series. Hence the overlap should be improved significantly by including 3.0 PN and higher-order conservative and radiative corrections, including spin terms [100,102,103,110,111].

In fact, our results indicate that higher-order PN corrections to the orbital motion may further increase the accuracy of the PN waveforms. Although, the PN expansion has not yet been shown to converge, we do find remarkably better agreement in ψ_4 between the PN and numerical waveforms when moving from a 2.5 PN EOM to a 3.5 EOM. This would appear to underscore the need for higher-order post-Newtonian calculations of both spin-orbit and spin-spin terms (especially in the EOM). Spin effects first appear at 1.5 PN order, producing the spin-orbit hang up effect [29,41]. Other spin effects, such as those due to precession, generate more subtle effects in the waveforms, and require higher-order PN corrections to accurately model (while subtle, these effects are also responsible for the very large kicks seen in spinning binaries with the spins oriented in the orbital plane). Our results seem to indicate that calculating these higher-order correction may prove to be invaluable for generating waveform templates from generic black-binary configurations. As a final point, we note that in this paper we have begun the exploration of the comparison PN and NR waveforms for generic black-hole-binary configurations, and other effects may yet be discovered that demonstrate further differences in the predictions of PN and NR waveforms

in other regions of the vast black-hole-binary parameter space.

ACKNOWLEDGMENTS

We thank E. Berti, A. Buonanno, A. Gopakumar, and R. Porto for careful review of the manuscript, and we thank B. Krishnan for suggesting the technique to calculate h from ψ_4. We thank the referees for their many helpful suggestions and insights, which have greatly improved the paper. We gratefully acknowledge NSF for financial support from Grants No. PHY-0722315, No. PHY-0653303, No. PHY 0714388, and No. PHY 0722703; and NASA for financial support from Grants No. NASA 07-ATFP07-0158 and No. HST-AR-11763.01. Computational resources were provided by Lonestar cluster at TACC and by NewHorizons at RIT.

APPENDIX A: TRANSFORMATION OF THE (ℓ, m) MODES OF SPIN-WEIGHTED FIELDS UNDER ARBITRARY ROTATIONS

Here we consider the spin-weighted spherical harmonics in two different angular coordinate systems, (θ, ϕ) and (θ', ϕ'), related to each other by a simple rotation. For convenience, we will use Ω to denote the coordinates (θ, ϕ) and $d\Omega = \sin\theta d\theta d\phi$ to denote the volume element on the unit sphere. To construct spin-weighted functions, we need to define a null dyad q^A on the unit sphere obeying $q^A q_A = 0$ and $q^A \bar{q}_A = 2$ (indices are raised and lowered with the unit sphere metric). Here we will use $q^A = \partial_\theta + i/\sin\theta\partial_\phi$ (see [112] for a review of the subject). Any two choices for the dyad q^A and q'^A can differ by at most a phase factor, i.e. $q'^A = e^{i\chi} q^A$. A spin-weight s field J transforms as $J \rightarrow J' = e^{is\chi} J$ under this change in spin basis. Of relevance here are the two dyads $q^A = \partial_\theta + i/\sin\theta\partial_\phi$ and $q'^A = \partial_{\theta'} + i/\sin\theta'\partial_{\phi'}$. The choice of q^A fixes the $\eth$ operator on spin-weighted fields.

The spin-weighted spherical harmonics are constructed as follows [108],

$$Y^s_{\ell m}(\Omega) = \sqrt{\frac{(\ell - |s|)!}{(\ell + |s|)!}} \begin{cases} (-1)^s \eth^s Y_{\ell m}(\Omega) & \text{if } s > 0 \\ \bar{\eth}^{|s|} Y_{\ell m}(\Omega) & \text{if } s < 0 \end{cases}, \quad \text{(A1)}$$

where

$$\eth f = \partial_\theta f + \frac{i}{\sin\theta}\partial_\phi f - sf\cot\theta, \qquad \bar{\eth} f = \partial_\theta f - \frac{i}{\sin\theta}\partial_\phi f + sf\cot\theta, \quad \text{(A2)}$$

for a function f of spin-weight s. In the Ω' coordinates and the corresponding q'^A spin basis. Equations (A1) and (A2) take on an identical form, but with the Ω coordinates replaced with the Ω' coordinates. Let J be a spin-weighted s field of arbitrary spin weight that can be decomposed into spin-weighted spherical harmonics. That is,

$$J = \sum_{\ell=|s|}^{\infty} \sum_{m=-\ell}^{\ell} J_{\ell m} Y^s_{\ell m}(\Omega). \quad \text{(A3)}$$

We define a spin-zero potential j, such that

$$j = \sum_{\ell=|s|}^{\infty} \sum_{m=-\ell}^{\ell} j_{\ell m} Y_{\ell m}(\Omega), \quad \text{(A4)}$$

where

$$j_{\ell m} = J_{\ell m} \sqrt{\frac{(\ell - |s|)!}{(\ell + |s|)!}} p, \quad \text{(A5)}$$

and $p = (-1)^s$ if $s > 0$ and $p = 1$ otherwise. Hence

$$J = \begin{cases} \eth^s j & \text{if } s > 0 \\ \bar{\eth}^{|s|} j & \text{if } s < 0 \end{cases}. \quad \text{(A6)}$$

Under a change of spin basis, $J \rightarrow J' = e^{is\chi} J$ but $j \rightarrow j' = j$. Thus

$$J' = \begin{cases} \eth'^s j & \text{if } s > 0 \\ \bar{\eth}'^{|s|} j & \text{if } s < 0 \end{cases}, \quad \text{(A7)}$$

and

$$J' = \sum_{\ell=|s|}^{\infty} \sum_{m=-\ell}^{\ell} \sqrt{\frac{(\ell + |s|)!}{(\ell - |s|)!}}\, p j'_{\ell m} Y'^s_{\ell m}(\Omega'), \quad \text{(A8)}$$

where

$$j'_{\ell m} = \int j \overline{Y'_{\ell m}(\Omega')} d\Omega'. \quad \text{(A9)}$$

Thus

$$J_{\ell m} = j_{\ell m} \sqrt{\frac{(\ell + |s|)!}{(\ell - |s|)!}} p, \qquad J'_{\ell m} = j'_{\ell m} \sqrt{\frac{(\ell + |s|)!}{(\ell - |s|)!}} p, \quad \text{(A10)}$$

where

$$J'_{\ell m} = \int J' \overline{Y'^s_{\ell m}(\Omega')} d\Omega', \quad \text{(A11)}$$

and hence we can determine how the modes of J mix under a rotation of the coordinates by looking at the modes of j.

It was shown in [108] that the relationship between the spherical harmonic modes $Y_{\ell m}(\Omega)$ and $Y'_{\ell m}(\Omega')$, where the Ω' coordinates are obtained from the Ω coordinates by a rotation described by the Euler angles α, β, γ in Sec. IV, is given by

$$Y_{\ell m}(\Omega) = \sum_{m'=-\ell}^{\ell} e^{-i(m'\alpha + m\gamma)} d^{\ell}_{m' m}(-\beta) Y'_{\ell m'}(\Omega'), \quad \text{(A12)}$$

and hence

$$j_{\ell m} = \int j\overline{Y_{\ell m}(\Omega)}d\Omega = \int j\overline{Y_{\ell m}(\Omega)}d\Omega'$$
$$= \int j \sum_{m'=-\ell}^{\ell} e^{i(m'\alpha+m\gamma)} d^{\ell}_{m'm}(-\beta)\overline{Y'_{\ell m'}(\Omega')}d\Omega'$$
$$= \sum_{m'=-\ell}^{\ell} e^{i(m'\alpha+m\gamma)} d^{\ell}_{m'm}(-\beta) j'_{\ell m'}. \quad \text{(A13)}$$

Finally, using Eq. (A10) we get

$$J_{\ell m} = \sum_{m'=-\ell}^{\ell} e^{i(m'\alpha+m\gamma)} d^{\ell}_{m'm}(-\beta) J'_{\ell m}, \quad \text{(A14)}$$

which is independent of the spin weight of J.

[1] A. A. Abramovici, W. Althouse, R. P. Drever, Y. Gursel, S. Kawamura, F. Raab, D. Shoemaker, L. Sievers, R. Spero, K. S. Thorne *et al.*, Science **256**, 325 (1992).
[2] F. Acernese *et al.* (VIRGO), Classical Quantum Gravity **21**, S385 (2004).
[3] F. Pretorius, Phys. Rev. Lett. **95**, 121101 (2005).
[4] M. Campanelli, C. O. Lousto, P. Marronetti, and Y. Zlochower, Phys. Rev. Lett. **96**, 111101 (2006).
[5] J. G. Baker, J. Centrella, D.-I. Choi, M. Koppitz, and J. van Meter, Phys. Rev. Lett. **96**, 111102 (2006).
[6] M. Campanelli, Classical Quantum Gravity **22**, S387 (2005).
[7] F. Herrmann, D. Shoemaker, and P. Laguna, AIP Conf. Proc. **873**, 89 (2006).
[8] J. G. Baker *et al.*, Astrophys. J. **653**, L93 (2006).
[9] C. F. Sopuerta, N. Yunes, and P. Laguna, Phys. Rev. D **74**, 124010 (2006).
[10] J. A. González, U. Sperhake, B. Brugmann, M. Hannam, and S. Husa, Phys. Rev. Lett. **98**, 091101 (2007).
[11] C. F. Sopuerta, N. Yunes, and P. Laguna, Astrophys. J. **656**, L9 (2007).
[12] F. Herrmann, I. Hinder, D. Shoemaker, and P. Laguna, AIP Conf. Proc. **873**, 89 (2006).
[13] F. Herrmann, I. Hinder, D. Shoemaker, and P. Laguna, Classical Quantum Gravity **24**, S33 (2007).
[14] F. Herrmann, I. Hinder, D. Shoemaker, P. Laguna, and R. A. Matzner, Astrophys. J. **661**, 430 (2007).
[15] M. Campanelli, C. O. Lousto, Y. Zlochower, and D. Merritt, Astrophys. J. **659**, L5 (2007).
[16] M. Koppitz *et al.*, Phys. Rev. Lett. **99**, 041102 (2007).
[17] D.-I. Choi *et al.*, Phys. Rev. D **76**, 104026 (2007).
[18] J. A. González, M. D. Hannam, U. Sperhake, B. Brugmann, and S. Husa, Phys. Rev. Lett. **98**, 231101 (2007).
[19] J. G. Baker *et al.*, Astrophys. J. **668**, 1140 (2007).
[20] M. Campanelli, C. O. Lousto, Y. Zlochower, and D. Merritt, Phys. Rev. Lett. **98**, 231102 (2007).
[21] E. Berti *et al.*, Phys. Rev. D **76**, 064034 (2007).
[22] W. Tichy and P. Marronetti, Phys. Rev. D **76**, 061502 (2007).
[23] F. Herrmann, I. Hinder, D. M. Shoemaker, P. Laguna, and R. A. Matzner, Phys. Rev. D **76**, 084032 (2007).
[24] B. Brugmann, J. A. Gonzalez, M. Hannam, S. Husa, and U. Sperhake, Phys. Rev. D **77**, 124047 (2008).
[25] J. D. Schnittman *et al.*, Phys. Rev. D **77**, 044031 (2008).
[26] B. Krishnan, C. O. Lousto, and Y. Zlochower, Phys. Rev. D **76**, 081501 (2007).
[27] K. Holley-Bockelmann, K. Gultekin, D. Shoemaker, and N. Yunes, arXiv:0707.1334.
[28] D. Pollney *et al.*, Phys. Rev. D **76**, 124002 (2007).
[29] S. Dain, C. O. Lousto, and Y. Zlochower, Phys. Rev. D **78**, 024039 (2008).
[30] I. H. Redmount and M. J. Rees, Comments Astrophys. **14**, 165 (1989).
[31] D. Merritt, M. Milosavljevic, M. Favata, S. A. Hughes, and D. E. Holz, Astrophys. J. **607**, L9 (2004).
[32] A. Gualandris and D. Merritt, arXiv:0708.0771.
[33] R. C. Kapoor, Pramana **7**, 334 (1976).
[34] T. Bogdanovic, C. S. Reynolds, and M. C. Miller, arXiv: astro-ph/0703054.
[35] A. Loeb, Phys. Rev. Lett. **99**, 041103 (2007).
[36] E. W. Bonning, G. A. Shields, and S. Salviander, arXiv:0705.4263.
[37] S. Komossa, H. Zhou, and H. Lu, Astrophys. J. Lett. **678**, L81 (2008).
[38] S. Komossa and D. Merritt, Astrophys. J. **683**, L21 (2008).
[39] M. Campanelli, C. O. Lousto, and Y. Zlochower, Phys. Rev. D **73**, 061501(R) (2006).
[40] J. G. Baker, J. Centrella, D.-I. Choi, M. Koppitz, and J. van Meter, Phys. Rev. D **73**, 104002 (2006).
[41] M. Campanelli, C. O. Lousto, and Y. Zlochower, Phys. Rev. D **74**, 041501(R) (2006).
[42] M. Campanelli, C. O. Lousto, and Y. Zlochower, Phys. Rev. D **74**, 084023 (2006).
[43] M. Campanelli, C. O. Lousto, Y. Zlochower, B. Krishnan, and D. Merritt, Phys. Rev. D **75**, 064030 (2007).
[44] F. Pretorius, Classical Quantum Gravity **23**, S529 (2006).
[45] F. Pretorius and D. Khurana, Classical Quantum Gravity **24**, S83 (2007).
[46] J. G. Baker, J. R. van Meter, S. T. McWilliams, J. Centrella, and B. J. Kelly, Phys. Rev. Lett. **99**, 181101 (2007).
[47] B. Brugmann *et al.*, Phys. Rev. D **77**, 024027 (2008).
[48] A. Buonanno, G. B. Cook, and F. Pretorius, Phys. Rev. D **75**, 124018 (2007).
[49] J. G. Baker *et al.*, Phys. Rev. D **75**, 124024 (2007).
[50] M. A. Scheel *et al.*, Phys. Rev. D **74**, 104006 (2006).
[51] J. G. Baker, M. Campanelli, F. Pretorius, and Y. Zlochower, Classical Quantum Gravity **24**, S25 (2007).
[52] P. Marronetti *et al.*, Classical Quantum Gravity **24**, S43 (2007).

[53] H. P. Pfeiffer *et al.*, Classical Quantum Gravity **24**, S59 (2007).
[54] U. Sperhake, V. Cardoso, F. Pretorius, E. Berti, and J. A. Gonzalez, Phys. Rev. Lett. **101**, 161101 (2008).
[55] M. Hannam, S. Husa, D. Pollney, B. Brugmann, and N. O'Murchadha, Phys. Rev. Lett. **99**, 241102 (2007).
[56] M. Hannam, S. Husa, F. Ohme, B. Brugmann, and N. O'Murchadha, Phys. Rev. D **78**, 064020 (2008).
[57] J. D. Brown, Phys. Rev. D **77**, 044018 (2008).
[58] D. Garfinkle, C. Gundlach, and D. Hilditch, Classical Quantum Gravity **25**, 075007 (2008).
[59] M. Campanelli, C. O. Lousto, and Y. Zlochower, arXiv:0811.3006.
[60] Z. B. Etienne, J. A. Faber, Y. T. Liu, S. L. Shapiro, K. Taniguchi, and T. W. Baumgarte, Phys. Rev. D **77**, 084002 (2008).
[61] T. Yamamoto, M. Shibata, and K. Taniguchi, Phys. Rev. D **78**, 064054 (2008).
[62] M. Campanelli, C. O. Lousto, and Y. Zlochower, Phys. Rev. D **77**, 101501(R) (2008).
[63] C. O. Lousto and Y. Zlochower, Phys. Rev. D **77**, 024034 (2008).
[64] J. Healy *et al.*, Phys. Rev. Lett. **102**, 041101 (2009).
[65] Y. Pan *et al.*, Phys. Rev. D **77**, 024014 (2008).
[66] A. Buonanno *et al.*, Phys. Rev. D **76**, 104049 (2007).
[67] T. Damour, A. Nagar, E. N. Dorband, D. Pollney, and L. Rezzolla, Phys. Rev. D **77**, 084017 (2008).
[68] T. Damour, A. Nagar, M. Hannam, S. Husa, and B. Bruegmann, Phys. Rev. D **78**, 044039 (2008).
[69] M. Boyle *et al.*, Phys. Rev. D **78**, 104020 (2008).
[70] P. Ajith *et al.*, Phys. Rev. D **77**, 104017 (2008).
[71] M. Hannam, S. Husa, U. Sperhake, B. Brugmann, and J. A. Gonzalez, Phys. Rev. D **77**, 044020 (2008).
[72] I. Hinder, F. Herrmann, P. Laguna, and D. Shoemaker, arXiv:0806.1037.
[73] L. Gualtieri, E. Berti, V. Cardoso, and U. Sperhake, Phys. Rev. D **78**, 044024 (2008).
[74] M. Hannam, S. Husa, B. Bruegmann, and A. Gopakumar, Phys. Rev. D **78**, 104007 (2008).
[75] D. Shoemaker, B. Vaishnav, I. Hinder, and F. Herrmann, Classical Quantum Gravity **25**, 114047 (2008).
[76] B. Vaishnav, I. Hinder, F. Herrmann, and D. Shoemaker, Phys. Rev. D **76**, 084020 (2007).
[77] S. Brandt and B. Brügmann, Phys. Rev. Lett. **78**, 3606 (1997).
[78] M. Ansorg, B. Brügmann, and W. Tichy, Phys. Rev. D **70**, 064011 (2004).
[79] Y. Zlochower, J. G. Baker, M. Campanelli, and C. O. Lousto, Phys. Rev. D **72**, 024021 (2005).
[80] T. Nakamura, K. Oohara, and Y. Kojima, Prog. Theor. Phys. Suppl. **90**, 1 (1987).
[81] M. Shibata and T. Nakamura, Phys. Rev. D **52**, 5428 (1995).
[82] T. W. Baumgarte and S. L. Shapiro, Phys. Rev. D **59**, 024007 (1998).
[83] P. Marronetti, W. Tichy, B. Brugmann, J. Gonzalez, and U. Sperhake, Phys. Rev. D **77**, 064010 (2008).
[84] E. Schnetter, S. H. Hawley, and I. Hawke, Classical Quantum Gravity **21**, 1465 (2004).
[85] M. Alcubierre, B. Brügmann, P. Diener, M. Koppitz, D. Pollney, E. Seidel, and R. Takahashi, Phys. Rev. D **67**, 084023 (2003).
[86] C. Gundlach and J. M. Martin-Garcia, Phys. Rev. D **74**, 024016 (2006).
[87] J. Thornburg, Classical Quantum Gravity **21**, 743 (2004).
[88] O. Dreyer, B. Krishnan, D. Shoemaker, and E. Schnetter, Phys. Rev. D **67**, 024018 (2003).
[89] M. Campanelli and C. O. Lousto, Phys. Rev. D **59**, 124022 (1999).
[90] C. O. Lousto and Y. Zlochower, Phys. Rev. D **76**, 041502 (R) (2007).
[91] M. Boyle *et al.*, Phys. Rev. D **76**, 124038 (2007).
[92] S. Husa, M. Hannam, J. A. Gonzalez, U. Sperhake, and B. Brugmann, Phys. Rev. D **77**, 044037 (2008).
[93] L. E. Kidder, Phys. Rev. D **52**, 821 (1995).
[94] B. J. Kelly, W. Tichy, M. Campanelli, and B. F. Whiting, Phys. Rev. D **76**, 024008 (2007).
[95] W. Tichy, B. Bruegmann, M. Campanelli, and P. Diener, Phys. Rev. D **67**, 064008 (2003).
[96] C. O. Lousto and Y. Zlochower, Phys. Rev. D **77**, 044028 (2008).
[97] C. O. Lousto and Y. Zlochower, Phys. Rev. D **79**, 064018 (2009).
[98] A. Buonanno, Y. Chen, and T. Damour, Phys. Rev. D **74**, 104005 (2006).
[99] T. Damour, P. Jaranowski, and G. Schafer, Phys. Rev. D **77**, 064032 (2008).
[100] J. Steinhoff, S. Hergt, and G. Schafer, Phys. Rev. D **77**, 081501(R) (2008).
[101] R. A. Porto and I. Z. Rothstein, Phys. Rev. Lett. **97**, 021101 (2006).
[102] R. A. Porto and I. Z. Rothstein, arXiv:0712.2032.
[103] R. A. Porto and I. Z. Rothstein, Phys. Rev. D **78**, 044012 (2008).
[104] A. H. Mroue, L. E. Kidder, and S. A. Teukolsky, Phys. Rev. D **78**, 044004 (2008).
[105] A. Buonanno, Y.-b. Chen, and M. Vallisneri, Phys. Rev. D **67**, 024016 (2003).
[106] R. V. Wagoner and C. M. Will, Astrophys. J. **210**, 764 (1976).
[107] L. Blanchet, G. Faye, B. R. Iyer, and S. Sinha, Classical Quantum Gravity **25**, 165003 (2008).
[108] J. N. Goldberg, A. J. MacFarlane, E. T. Newman, F. Rohrlich, and E. C. G. Sudarshan, J. Math. Phys. (N.Y.) **8**, 2155 (1967).
[109] E. Berti, V. Cardoso, J. A. Gonzalez, U. Sperhake, and B. Brugmann, Classical Quantum Gravity **25**, 114035 (2008).
[110] R. A. Porto and I. Z. Rothstein, Phys. Rev. D **78**, 044013 (2008).
[111] J. Steinhoff, G. Schafer, and S. Hergt, Phys. Rev. D **77**, 104018 (2008).
[112] R. Gomez, L. Lehner, P. Papadopoulos, and J. Winicour, Classical Quantum Gravity **14**, 977 (1997).